

An Intrinsic Geometrical Approach for Statistical Process Control of Surface and Manifold Data

Xueqi Zhao

Enrique del Castillo*

Engineering Statistics and Machine Learning Laboratory

Department of Industrial and Manufacturing Engineering and Dept. of Statistics

The Pennsylvania State University, University Park, PA 16802, USA

July 19, 2022

Abstract

This paper presents a new method for statistical process control (SPC) of a discrete part manufacturing system based on intrinsic differential-geometric properties of the parts. The approach estimates the spectrum of the Laplace-Beltrami (LB) operator of the scanned parts and uses a multivariate nonparametric control chart for on-line process control. An intrinsic method has the computational advantage of avoiding the difficult part registration problem. Our proposal brings SPC closer to computer vision and computer graphics methods, but the SPC problem differs in that small changes in shape or size of the parts need to be detected without completely filtering noise, which, if incremented, can be a signal to detect as well, while keeping a controllable false alarm rate. Both an on-line or “phase II” method and a scheme for starting up in the absence of prior data (“phase I”) are presented, both based on recent work on permutation-based SPC methods. The run length and detection performance of the phase II and phase I methods are investigated. Comparison with a simpler SPC method based on registration of parts shows the LB spectrum methods to be much more sensitive to rapidly detect small changes in shape and size, including the practical case when the sequence of part surface datasets is in the form of large, unequal size meshes. A post-alarm diagnostic method to investigate the location of defects on the surface of a part is also presented. The methods can be applied to point cloud, mesh, and even voxel metrology data.

Keywords: Laplace-Beltrami operator, Permutation tests, CAD, manifold data analysis.

*Corresponding author. Dr. Castillo is Distinguished Professor of Industrial & Manufacturing Engineering and Professor of Statistics. e-mail: exd13@psu.edu

Contents

1	Introduction	3
2	Preliminaries	5
3	The spectrum of the Laplace-Beltrami operator to characterize the geometry of a 3D object	11
3.1	Approximating the LB operator and its spectrum	12
3.2	Computation and stability of the discrete LB operator spectrum	16
4	Using the estimated LB spectrum as a tool for SPC	18
4.1	Permutation tests based on the LB spectrum	19
4.2	On-line SPC scheme (“Phase II”)	22
4.3	Run length behavior	24
5	Post alarm diagnostics	27
6	A permutation-based SPC scheme for “Phase I”	28
7	Discussion: other intrinsic geometrical statistics for process control	31
7.1	Heat kernel and diffusion distances	31
7.2	Other spectral distances	34
8	Conclusions and further work	35

1 Introduction

Widespread use of modern sensors in engineering and industry in recent times has resulted not only in bigger datasets but also in more complex datasets. Statistical Process Control (SPC) is an area that has witnessed increased sophistication in metrology accompanied by increased complexity in the resulting data sets related to production or manufacturing processes (Colosimo, 2018). We consider the case non-contact sensors collect point cloud and mesh data formed by thousands of points $\mathbf{x} = (x_1, x_2, x_3)' \in \mathbb{R}^3$ which actually lie in what is a 2-dimensional manifold, the actual surface of the object or part produced. Due to manufacturing and measurement errors, the observed surface will deviate from the target or nominal surface, given by the design of the part, usually available in some Computer Aided Design (CAD) file. In this paper, we present fundamentally new differential-geometric methods for performing SPC of a manufacturing system producing discrete parts from their associated scanned datasets. The method can be applied to mesh (triangulation), point cloud, and even voxel (tetrahedralization) datasets, and is based on techniques some of which have been used in recent years in Computer Graphics, Computer Vision, and Machine Learning.

Traditional treatment of 2 and 3-dimensional point cloud datasets in Statistics pertains to the field of Statistical Shape Analysis (SSA, Kendall (1984); Dryden & Mardia (2016); for applications in manufacturing see del Castillo & Colosimo (2011)). In SSA, the m -point cloud data are represented by a configuration matrix $\mathbf{X} \in \mathbb{R}^{m \times n}$ with $n = 2$ or 3 . The *Shape* of an object is defined as the geometrical information in \mathbf{X} that remains after discounting the effect of similarity transformations usually excepting reflections (translations, rotations and dilations). To make inferences on the shape of N objects, the Generalized Procrustes Algorithm, GPA, is first applied. The GPA registers or superimposes all the N objects by finding scaling factors $\beta_i \in \mathbb{R}$, rotation matrices $\mathbf{\Gamma}_i \in SO(n)$ (the special orthogonal group, which exclude reflections and have determinant one) and n -dimensional translation vectors $\boldsymbol{\gamma}_i, i = 1, \dots, N$, such that they minimize the sum of squared full procrustes distances between all pairs of configuration matrices ($d_F(\mathbf{X}_i, \mathbf{X}_j)$):

$$\begin{aligned} G(\mathbf{X}_1, \mathbf{X}_2, \dots, \mathbf{X}_N) &= \min_{\beta_i, \mathbf{\Gamma}_i, \boldsymbol{\gamma}_i} \frac{1}{N} \sum_{i=1}^N \sum_{j=i+1}^N \|\beta_i \mathbf{X}_i \mathbf{\Gamma}_i + \mathbf{1}_m \boldsymbol{\gamma}'_i - (\beta_j \mathbf{X}_j \mathbf{\Gamma}_j + \mathbf{1}_m \boldsymbol{\gamma}'_j)\|^2 \\ &= \frac{1}{N} \sum_{i=1}^N \sum_{j=i+1}^N d_F^2(\mathbf{X}_i, \mathbf{X}_j) \end{aligned} \quad (1)$$

where $\mathbf{1}_m$ is a vector of m ones. Constraints must be added to avoid the trivial solution where all parameters are zero (Dryden & Mardia, 2016). Other shape analysis methods based on euclidean distances between the points (Lele, 1993) require large distance matrices and will not be discussed here.

The problem of registering two three dimensional objects with a large but *different* number of (non-corresponding) points has been known for a long time in the computer vision literature, where the Iterated Closest Point (ICP) algorithm (Besl & McKay (1992); Zhang (1992)) is a standard. Consider the configurations of two distinct *unlabeled* objects

$\mathbf{X}_q \in \mathbb{R}^{m_1 \times n}$ and $\mathbf{X}_p \in \mathbb{R}^{m_2 \times n}$ (with $n = 3$), not necessarily having the same pose and assume $m_1 \leq m_2$. Let $\mathbf{M} \in \mathbb{R}^{m_1 \times m_2}$ with $M_{ij} = 1$ if $\mathbf{x}_{q,i} \in \mathbf{X}_q$ is matched with point $\mathbf{x}_{p,j} \in \mathbf{X}_p$, and zero otherwise. The objects may be located and oriented differently in space, and hence the problem is not only to find the correspondences but also a rigid body transformation $T(\mathbf{x}) = \mathbf{\Gamma}\mathbf{x} + \boldsymbol{\gamma}$ that registers the two objects such that we

$$\min_{\mathbf{M}, \mathbf{\Gamma}, \boldsymbol{\gamma}} L(\mathbf{M}, \mathbf{\Gamma}, \boldsymbol{\gamma}) = \min_{\mathbf{M}, \mathbf{\Gamma}, \boldsymbol{\gamma}} \sum_{i=1}^{m_1} \sum_{j=1}^{m_2} M_{ij} C(\mathbf{\Gamma}\mathbf{x}_{q,i} + \boldsymbol{\gamma}, \mathbf{x}_{p,j}) \quad (2)$$

subject to $\sum_{j=1}^{m_2} M_{ij} = 1, i = 1, \dots, m_1$, and $M_{ij} = 0$ or 1 , where $C(\mathbf{\Gamma}\mathbf{x}_1 + \boldsymbol{\gamma}, \mathbf{x}_2)$ is the cost of matching point \mathbf{x}_1 to point \mathbf{x}_2 . This is a hard non-linear discrete optimization problem. Existing heuristics differ by choosing different cost functions C . In the ICP method, $C(\mathbf{\Gamma}\mathbf{x}_{q,i} + \boldsymbol{\gamma}, \mathbf{x}_{p,j}) = \|\mathbf{\Gamma}\mathbf{x}_{q,i} + \boldsymbol{\gamma} - \mathbf{x}_{p,j}\|$, the euclidean distance between $\mathbf{x}_{q,i}$ in \mathbf{X}_q and the *closest point* $\mathbf{x}_{p,j}$ in \mathbf{X}_p .

Commercial Computer Aided Design (CAD) and inspection software use variants of the ICP method to align the cloud points of each scanned object and that of the CAD file, in order to determine regions in the manufactured part that differ from nominal. To do this, a CAD model, usually in the form of NURBS curves, is sampled to form a mesh or triangulation, and then the alignment of the CAD and scanned part triangulations can be performed. Figure 1 shows an instance of a metal part CAD model and two color-coded comparisons between the CAD model and the 3D-printed part. This is actually voxel data, not mesh or point cloud data on the surface of the object, but the registration problem is essentially identical.

A first approach to Statistical Process Control based on surface (and in general, point cloud and voxel) data can be based on monitoring the deviations from nominal shown in Figure 1 after applying the ICP method, similarly to a “DNOM” (deviation from nominal) control chart (see e.g., Farnum (1994)). The deviations from nominal are vectors, and either their norm or their individual components could be used for SPC. The optimal value of the ICP statistic (2), $L(\mathbf{M}, \mathbf{\Gamma}, \boldsymbol{\gamma})$ between CAD file and each scanned part could be monitored on-line, for instance, to provide a “generic” SPC mechanism against a wide variety of unanticipated out of control states in the geometry of a part, in a similar sense to what Box and Ramírez thought of univariate Shewhart charts (Box & Ramírez, 1992), with other SPC or diagnostic mechanisms added to detect more specific, or more localized defects on the part. As far as we know, this simple strategy has not been proposed in the literature, so we consider it and contrast it with the new intrinsic differential-geometrical methods that conform our main contribution. We also discuss other registration-based SPC methods that instead of ICP use spectral distances in section 7.

Our approach brings SPC of discrete-part manufacturing closer to the Computer Graphics field. The differential-geometrical approaches we propose are based on techniques popular in computer graphics to characterize 3D objects, and these methods have also been used in machine learning of general manifolds of much higher dimension than the 2-manifolds (surfaces) we focus in this paper. In computer graphics and computer vision applications, however, the problem to solve is the identification of large differences between the shapes of objects for classification purposes or to match a query object, tasks that a (patient) human can in principle perform. Here, in contrast, we focus in detecting considerable smaller

differences (sometimes not perceptible to the eye) between a sequence of objects which the manufacturer is trying to make as identical to each other as possible, hence differences will tend to be rather small. A further difficulty in SPC is that, in addition to detecting changes in the mean shape of an object, a noise increment should be considered a process signature change to be detected, rather than a signal that must be filtered and ignored as in Computer Vision, where shape identification methods that are robust with respect to noise are typically sought.

In this paper, we follow the traditional SPC paradigm. The main goal is detection of significant part to part differences with respect to historical variation because they may indicate a manufacturing process problem, and the aim is to detect “assignable causes of variation” as soon as possible, while avoiding false alarms using a statistical monitoring scheme. The paper is organized as follows. Section 2 first reviews some preliminary mathematical concepts in order to present the new differential-geometric SPC methods, including the main operator we will use, the Laplace-Beltrami (LB) operator, and its spectrum. The spectrum of the LB operator needs to be estimated from data, and section 3 discusses methods to do so. The spectral methods we utilize are also popular in the analysis of social networks, and as it will be shown there is a close connection between the combinatorial or graph Laplacian and the discretized Laplace-Beltrami operator we utilize, since both are based on a graph. Section 4 presents the main practical results, where a specific distribution-free multivariate chart is used to monitor a process with respect to an in-control reference data set (i.e. “phase II” in SPC) using the spectrum of the estimated discrete LB operator of a sequence of scanned parts. We show how the spectral methods have greater sensitivity to detect general out of control conditions in a discrete-part manufacturing process than using the deviations from nominal ICP method sketched above. As additional post SPC alarm diagnostics, in section 5 we investigate the use of ICP to localize the occurrence of defects on a part. To make the presentation of our SPC proposal complete, section 6 discusses a method based on the spectrum of the LB operator for the first phase (“phase I”) when monitoring a process in the absence of prior in-control data. Section 7 contains a discussion of alternative spectral distances popular in Computer Graphics that have received recent attention in the Statistics literature and their potential use in SPC. The paper concludes with conclusions and some directions for further research.

2 Preliminaries

For completeness, we first define the Differential Geometric concepts we use in the sequence; for most of them see, e.g. Kreyszig (1991) or O’Neill (2006). In Differential Geometry, one begins with properties affecting the vicinity of a point on a surface and deduces properties governing the overall structure of the object under consideration.

We consider either surface or voxel data, which constitute datasets sampled from instances of a k -dimensional manifold ($k = 2$ or 3 , respectively) embedded in 3-dimensional Euclidean space. Informally, a manifold \mathcal{M} is a k -dimensional space that resembles \mathbb{R}^k

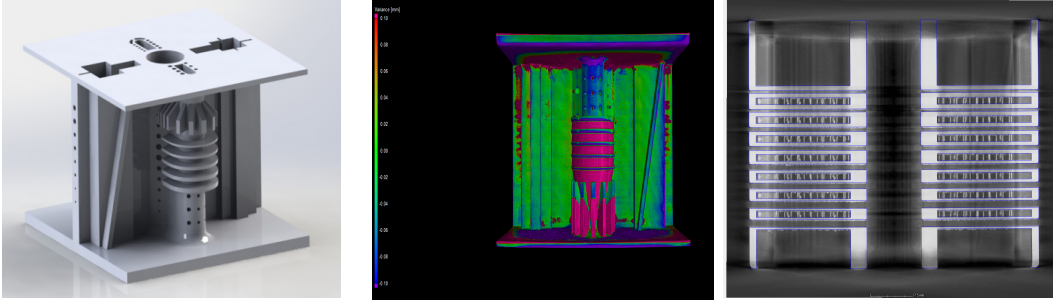


Figure 1: Left: CAD design 3D rendering of a metal part. Middle: CT image of the manufactured part with color contrast indicating differences in the x dimension between the CAD model and the actual part. The CT software registers the CAD model and actual part using the ICP algorithm and color codes the deviations from nominal for visualization. Right: internal view of actual manufactured part (voxel data obtained via a computed tomography (CT) machine).

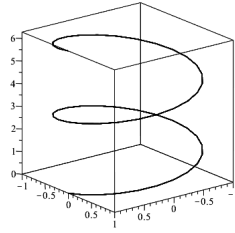


Figure 2: An instance of a parametric curve is the helicoidal curve defined by $\mathbf{p}(t) = (x(t) = \cos(t), y(t) = \sin(t), z(t) = t)$, where $t \in D \subset \mathbb{R}$ is the curve coordinate or parameter. Here the intrinsic dimension of the manifold is $k = 1$ with $x^1 = t$, while the ambient space dimension is $m = 3$.

(Euclidean space) on small domains around each of its points (we will assume \mathcal{M} is compact and connected). The manifold hypothesis, useful if true in machine learning and in engineering data, indicates that high (n -) dimensional data frequently lie on or near a lower, often curved k -dimensional manifold, where $k < n$. In smooth manifolds with an inner product, the so-called Riemannian manifolds, we can measure distances, areas, volumes, etc. If the manifold hypothesis holds, we say the *intrinsic* dimension of the data is k , and that the manifold is *embedded* in a n -dimensional *ambient* space. For manifold data, any n -dimensional point \mathbf{x} can be completely described by defining k local (intrinsic) coordinates or “parameters” x^1, x^2, \dots, x^k . For instance, consider a *parametric curve* in \mathbb{R}^3 , such as the helicoidal curve in Figure 2. This is an instance of a 1-manifold. In this paper, we will mostly consider data sampled from surfaces or 2-manifolds of manufactured parts, although all our methods are extendable to the case of 3-manifolds, i.e., voxel-data.

Definition 1. Any property of a manifold \mathcal{M} that can be computed without recourse to the ambient space coordinates, and instead is computed using only the intrinsic or local manifold coordinates x^1, \dots, x^k is said to be an *intrinsic geometrical property*, or simply, an *intrinsic property*, of \mathcal{M} .

Definition 2. Any geometrical property of an object that remains constant after application of a given transformation is said to be *invariant* with respect to that transformation.

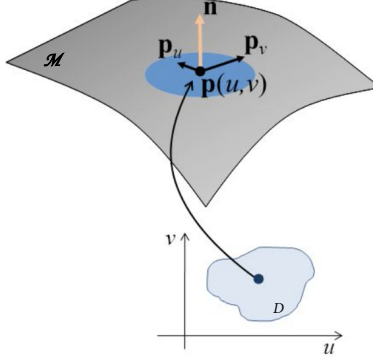


Figure 3: A parametrization of a surface, its surface differential vectors at a point $\mathbf{p}(u, v)$, \mathbf{p}_u and \mathbf{p}_v , the normal vector \mathbf{n} and the tangent plane at $\mathbf{p}(u, v)$, T_p , spanned by the differential vectors.

Intrinsic geometrical properties of a manifold in Euclidean space are invariant with respect to *rigid transformations* (rotations and translations, but not dilations), but the opposite is not true. For instance, Euclidean distances between points in a configuration matrix \mathbf{X} are invariant to rigid transformations but they are evidently not intrinsic. An instance of an intrinsic property is the geodesic distance between two points located on a manifold \mathcal{M} , which is therefore also invariant with respect to rigid transformations. In section 7, we discuss intrinsic distances other than the geodesic.

A well-known result in Differential Geometry indicates that intrinsic geometrical properties of a manifold depend only on the so-called *first fundamental form* of \mathcal{M} . For the 2-manifolds (surfaces) we mostly deal with in this paper, this quadratic form is defined as follows. Consider a parametric surface $\mathbf{p}(u, v) = (x(u, v), y(u, v), z(u, v))'$, $(u, v) \in D \subset \mathbb{R}^2$ (here $u = x^1, v = x^2$) which defines \mathcal{M} , a Riemannian 2-manifold. Define the surface differential vectors at $\mathbf{p}(u, v)$ as:

$$\mathbf{p}_u = \frac{\partial \mathbf{p}(u, v)}{\partial u} = \left(\frac{\partial x(u, v)}{\partial u}, \frac{\partial y(u, v)}{\partial u}, \frac{\partial z(u, v)}{\partial u} \right)'$$

and

$$\mathbf{p}_v = \frac{\partial \mathbf{p}(u, v)}{\partial v} = \left(\frac{\partial x(u, v)}{\partial v}, \frac{\partial y(u, v)}{\partial v}, \frac{\partial z(u, v)}{\partial v} \right)'$$

(see Figure 3.) Now define a parametric curve on \mathcal{M} , $\alpha(t) = \mathbf{p}(u(t), v(t))$ such that $\mathbf{p}(u_0, v_0) = \alpha(0)$ and use the chain rule:

$$\frac{d\alpha(t)}{dt} = \frac{\partial \mathbf{p}}{\partial u} \frac{du(t)}{dt} + \frac{\partial \mathbf{p}}{\partial v} \frac{dv(t)}{dt} = \mathbf{p}_u \frac{du(t)}{dt} + \mathbf{p}_v \frac{dv(t)}{dt}.$$

Finally, take the inner product (borrowed from \mathbb{R}^3):

$$\begin{aligned} I_p \left(\frac{d\alpha(t)}{dt} \right) &= \left\langle \frac{d\alpha(t)}{dt}, \frac{d\alpha(t)}{dt} \right\rangle = (ds)^2 \\ &= g_{11} \left(\frac{du(t)}{dt} \right)^2 + 2g_{12} \frac{du(t)}{dt} \frac{dv(t)}{dt} + g_{22} \left(\frac{dv(t)}{dt} \right)^2 \end{aligned}$$

where: $g_{11} = \langle \mathbf{p}_u, \mathbf{p}_u \rangle$ $g_{12} = \langle \mathbf{p}_u, \mathbf{p}_v \rangle$ $g_{22} = \langle \mathbf{p}_v, \mathbf{p}_v \rangle$. We then have the following.

Definition 3. The quadratic form $I_p(\alpha(t)') = (ds)^2$ is called the *first fundamental form* of the parametric surface $\mathbf{p}(u, v)$ describing \mathcal{M} . It provides a means to measure arc lengths, areas and angles on \mathcal{M} . It defines a new inner product for vectors on tangent planes $\langle, \rangle_{\mathcal{M}}$ and therefore, a *metric* on the surface, with associated matrix (tensor) \mathbf{g} :

$$\langle \mathbf{w}_1, \mathbf{w}_2 \rangle_{\mathcal{M}} = \mathbf{w}_1^T \mathbf{g} \mathbf{w}_2, \quad \mathbf{g} = \begin{pmatrix} g_{11} & g_{12} \\ g_{12} & g_{22} \end{pmatrix}.$$

In this sense, the ambient space induces a metric, the Riemannian metric, on the manifold \mathcal{M} . Since $|\mathbf{w}| = \sqrt{\langle \mathbf{w}, \mathbf{w} \rangle_{\mathcal{M}}}$, the length of a curve segment on \mathcal{M} is:

$$s(t) = \int_0^t \sqrt{ds^2} dt.$$

With the Riemannian metric \mathbf{g} , we can also compute differential operators acting on a function defined on \mathcal{M} , which are very useful for our purposes, i.e., for estimation, and therefore, statistical monitoring, of intrinsic geometrical properties of an object.

Definition 4. The *gradient* of a function on \mathbb{R}^n points in the direction of steepest ascent:

$$\nabla f = \left(\frac{\partial f}{\partial x_1}, \frac{\partial f}{\partial x_2}, \dots, \frac{\partial f}{\partial x_n} \right)$$

and creates a vector field in \mathbb{R}^n .

Definition 5. The *divergence* of a vector field \mathbf{F} in \mathbb{R}^n is given by:

$$\text{div } \mathbf{F} = \nabla \cdot \mathbf{F} = \frac{\partial F_1}{\partial x_1} + \frac{\partial F_2}{\partial x_2} + \dots + \frac{\partial F_n}{\partial x_n}$$

and measures the “quantity” of the outward flux of F from the infinitesimal neighborhood around each point p . This is a scalar-valued function that creates a scalar field.

Definition 6. The *Laplace operator* of a twice differentiable function $f : \mathbb{R}^n \rightarrow \mathbb{R}$ is minus the divergence of its gradient field:

$$\Delta f = -\text{div } \nabla f = -\sum_{i=1}^n \frac{\partial^2 f}{\partial x_i^2}$$

and measures the difference between $f(x)$ and the average $f(x)$ in a neighborhood around x . Given the second derivatives, it is a measure of curvature, and can be alternatively understood as minus the trace of the Hessian of $f(x)$.

Finally, we define the main differential-geometric operator we will use in the sequence, the Laplace Beltrami operator, widely used in Computer Graphics and Machine Learning (Belkin, 2003; Kimmel, 2004; Levy, 2006; Patané, 2014; Reuter *et al.*, 2006).

Definition 7. For a function $f : \mathcal{M} \rightarrow \mathbb{R}$, the *Laplace-Beltrami* (LB) operator (sometimes called the “second differential parameter of Beltrami”) is defined as:

$$\Delta_{\mathcal{M}} f = -\text{div}_{\mathcal{M}} \nabla_{\mathcal{M}} f$$

where $\text{div}_{\mathcal{M}}$ is the divergence taken on \mathcal{M} . For a point defined by a parametric surface $\mathbf{p}(u, v)$ the following relation holds:

$$\Delta_{\mathcal{M}}\mathbf{p}(u, v) = -\text{div}_{\mathcal{M}} \nabla_{\mathcal{M}}\mathbf{p}(u, v) = 2H \mathbf{n}(u, v) \in \mathbb{R}^3$$

where $\mathbf{n}(u, v)$ is the normal at the point $\mathbf{p}(u, v)$ on \mathcal{M} (see Figure 3) and H is the *mean curvature* of \mathcal{M} at \mathbf{p} , which equals the average of the maximum and minimum curvatures at \mathbf{p} . This relation provides a geometric interpretation of the action of the LB operator, which can be visualized as creating a vector field of normals on \mathcal{M} such that the “height” of the normal is twice the mean curvature of \mathcal{M} at that point.

The LB operator extends the definition of the Laplacian to functions defined on manifolds, and is an intrinsic measure of local curvature at a point. Its intrinsic nature can be seen from defining a local coordinate system (or parametrization) on the manifold $(\mathbf{x}(x^1, \dots, x^k))$, with $k = 2$ for surfaces). Then, the LB operator applied to a function $f(x^1, \dots, x^k) \in \mathcal{C}^2$ is defined as:

$$\Delta_{\mathcal{M}}f = -\frac{1}{\sqrt{\det(g)}} \sum_{j=1}^k \frac{\partial}{\partial x^j} \left(\sqrt{\det(g)} \sum_{i=1}^k g^{ij} \frac{\partial f}{\partial x^i} \right) \quad (3)$$

where g^{ij} are the elements of \mathbf{g}^{-1} and the minus sign is to be consistent with our definition. Appendix 1 illustrates how to compute the LB operator of a function defined on a 2-dimensional manifold using (3). The LB operator on f is therefore a function of elements in the metric tensor \mathbf{g} only, and thus it is intrinsic and invariant with respect to rigid transformations. As it will be discussed below, the spectrum of the LB operator contains considerable geometric information about the manifold, and is widely used for this reason in both machine learning and computer graphics/computer vision.

The LB operator emerges from the spatial part of the solution to the heat and wave partial differential equations, see Table 1. If \mathcal{M} has boundaries, the solution to the heat and wave equations requires additional conditions such as the so-called Dirichlet boundary condition $u(x, t) = 0$ for all $x \in \partial\mathcal{M}$ (so the boundary $\partial\mathcal{M}$ acts as an absolute refrigerator for all $t > 0$ in the case of the heat equation).

The Laplacian eigenvalue problem is

$$\Delta_{\mathcal{M}}f = \lambda f \quad (4)$$

sometimes called the Helmholtz partial differential equation, with an infinite number of eigenfunctions f and eigenvalue λ pairs. The collection of eigenvalues $\{\lambda_i\}_{i=0}^{\infty}$ is called the *spectrum* of the LB operator. Defining the inner product on the compact and connected manifold \mathcal{M} as $\langle f, g \rangle = \int_{\mathcal{M}} f(p)g(p)dp$ for $f, g \in L_2(\mathcal{M})$ (space of square integrable functions on \mathcal{M}), it can be seen that the LB operator is self-adjoint, i.e., $\langle \Delta f, g \rangle = \langle f, \Delta g \rangle$ and positive semi-definite ($\langle \Delta f, f \rangle \geq 0$). Furthermore, the eigenvalues are such that $0 = \lambda_1 \leq \lambda_2 \leq \lambda_3, \dots$ and the eigenfunctions form an orthonormal basis in $L_2(\mathcal{M})$, see Chavel (1984).

In case $\mathcal{M} = \mathbb{R}^2$, the eigenfunctions $f(u, v)_i$ satisfying the Helmholtz equation can be interpreted as the modes of vibration of a 2D membrane with resonant or natural

HEAT EQUATION	WAVE EQUATION
$\frac{\partial u(x,t)}{\partial t} = \Delta u(x,t)$	$\frac{\partial^2 u(x,t)}{\partial t^2} = \Delta u(x,t)$
Separate variables: $u(x,t) = f(x)g(t)$	
$f(x)g'(t) = \Delta f(x)g(t)$	$f(x)g''(t) = \Delta f(x)g(t)$
Divide both sides by $f(x)g(t)$	
$\frac{g'(t)}{g(t)} = \frac{\Delta f(x)}{f(x)} = \lambda$	$\frac{g''(t)}{g(t)} = \frac{\Delta f(x)}{f(x)} = \lambda$
$\Delta f(x) = \lambda f(x)$	$\Delta f(x) = \lambda f(x)$

Table 1: The Laplace-Beltrami operator emerges from the solution of both the heat (left column) and wave (right column) partial differential equations, obtained by simple separation of the time and spatial domains. It is assumed $u(x,t)$ is differentiable enough times in each argument for each equation. In both cases, the Helmholtz equation, solved by finding the eigensystem associated with the LB operator, is obtained from the spatial part of the solution.

frequencies λ_i . The question of whether one can determine the shape of the drum holding the membrane on its boundary from its spectrum entertained mathematical physicists for many years until it was shown by Gordon *et al.* (1992) that there are pairs of 2D drums that have the same spectrum, yet their shapes are different, see Figure 4. In general, for $\mathcal{M} \subset \mathbb{R}^3$, this result implies that the geometric information contained in the spectrum is not enough to uniquely identify the shape of the surface \mathcal{M} . However, these pairs of figures are always concave polygons and correspond segment by segment, so they are rare.

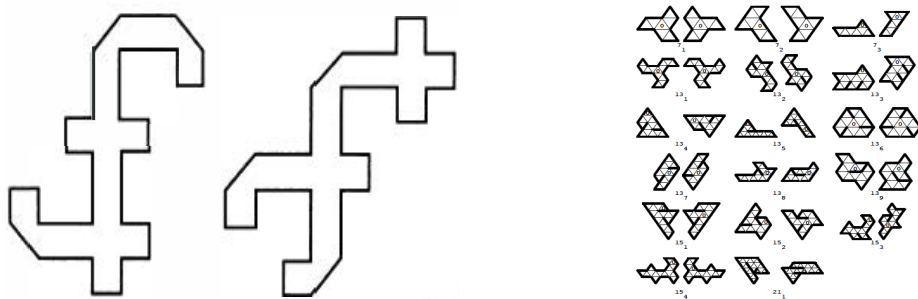


Figure 4: Left: Gordon *et al.* (1992) counterexample showing one cannot determine the shape of a drum from the spectrum of its membrane; this pair of shapes of “drums” are isospectral but not isometric (congruent). Right: Many other counterexamples of isospectral, not isometric pairs of planar figures from Buser *et al.* (1994). Fortunately, these counterexamples are rare, always formed by concave objects, made of simpler polygons that can be put in one to one correspondence.

The spectrum of the LB operator is always discrete, non-negative, and contains con-

siderable geometrical and topological information about a manifold that can be used for shape identification. For instance, for a surface:

$$\lim_{i \rightarrow \infty} \frac{\lambda_i}{i} = \frac{4\pi}{\text{Area}(\mathcal{M})} \quad (5)$$

(thus the area of \mathcal{M} can be inferred from the asymptotic slope of the spectrum, note λ_i is proportional to the index i). Another result shown in a classic paper by Kac (1966) is

$$\sum_{i=1}^{\infty} e^{-\lambda_i t} \leq \frac{\text{Area}(\mathcal{M})}{2\pi t}.$$

Also, the spectrum contains topological information about \mathcal{M} . For instance, one result showing dependency of the spectrum on topological information is that for a surface without boundary (Yang & S.T., 1980),

$$\lambda_1 \leq \frac{8\pi(\mathcal{G} + 1)}{\text{Area}(\mathcal{M})}$$

where \mathcal{G} is the genus of the surface (number of holes).

The spectrum changes in a continuous form with continuous changes of the shape of the manifold. Furthermore, scaling a surface \mathcal{M} by a factor of s changes the eigenvalues by $1/s^2$ (see Figure 5). It is possible to extract useful information from the lower part of the spectrum. According to Reuter *et al.* (2009), the LB operator spectrum of a manifold has more discrimination power than simpler measures like surface area. These authors provided examples of shapes with the same surface area but different spectrum. Topological data analysis tools can be applied to the eigenvectors in order to extract topological information such as the number of holes. We leave this for further research (see conclusions section).

3 The spectrum of the Laplace-Beltrami operator to characterize the geometry of a 3D object

The true spectrum of very few manifolds is known. One instance where it is known is the case of a unit sphere (Figure 5). Repeated eigenvalues are the result of perfect symmetries in the geometry of an object and are therefore rare in practice. To characterize the geometry of general 3D objects, such as discrete parts from a manufactured process, we need to use a discrete approximation of the LB operator based on a sample of points, possibly with adjacency information, forming a mesh.

In machine learning, LB operator-based methods have proved useful in both unsupervised and semi-supervised learning methods (e.g., see Belkin & Niyogi (2008)). For unsupervised learning, the spectrum of the LB operator is used. For semi-supervised learning, a function f defined on \mathcal{M} is observed at certain points—a point cloud dataset. The main goal is to fit this function, and an approximation to the LB operator is needed based on such dataset. Computer graphics and computer vision authors have also used the LB operator for shape classification (e.g., see Kimmel (2004); Levy (2006)).

3.1 Approximating the LB operator and its spectrum

For SPC of surface (2-manifold) data, we can make use of the geometric information encoded in the spectrum of the LB operator of a surface, which is invariant and intrinsic. The LB operator is linear, taking functions into functions. Eigenfunctions of the LB operator form a basis for the space of square integrable functions on \mathcal{M} . In the particular case \mathcal{M} is a circle (1-dimensional manifold) the corresponding basis functions consist of the usual Fourier harmonics $\sin(k\pi x)$ and $\cos(k\pi x)$. Applied to a differentiable function evaluated on a surface point x , $\Delta_{\mathcal{M}}f(x)$ returns a scalar. In practice, we have no expression for the surface \mathcal{M} , we only have a (large) sample of points from it. We can discretize the manifold \mathcal{M} based on the data, and an approximate, or *discrete LB operator* is obtained in the form of a matrix acting on vectors, returning a vector. One then works with the eigenvalues of the matrix which approximate the true spectrum of the manifold. There are different ways to discretize the manifold where the data lies. In computer graphics and machine learning, it is common to build a mesh or graph to represent the manifold, with the vertices representing the data points and the edges representing proximity relations that define the geometry of the manifold. A typical case in computer graphics are triangulations, sometimes generated automatically by non-contact sensors. If the data is in the form of a point cloud, a graph is also constructed from the nearest neighbors to each point. Finite-element methods (FEM) approximations of the LB operator for mesh data (Reuter *et al.*, 2006) and for voxel data (Reuter *et al.*, 2007) have also been developed, which increases the practical use of this differential geometry tool.

Motivation for some of the most popular LB operator approximations used for analyzing the shape of an object comes from the theory of heat diffusion and wave propagation in Physics (see Table 1). For instance, if the sensor data available has the form of a triangulation \mathcal{K} , the Mesh Laplacian approximation (Belkin *et al.*, 2008) is given by:

$$L_{\mathcal{K}}^t f(p_i) = \frac{1}{4\pi t^2} \sum_{T \in T_{\mathcal{K}}} \frac{A(T)}{3} \sum_{p_j \in V(T)} e^{-\|p_i - p_j\|^2/4t} (f(p_i) - f(p_j)), \quad j = 1, 2, \dots, m \quad (6)$$

where $T_{\mathcal{K}}$ denotes the set of all triangles in the mesh, $A(T)$ denotes the area of triangle T , and $V(T)$ denotes the set of vertices in triangle T . The discrete LB operator contains the quantity

$$k_t(x, y) = \frac{1}{4\pi t} e^{-\|x - y\|^2/4t}$$

called the heat kernel, which can be thought to be the amount of heat that is transferred from x to y in time t if there is a unit heat source at x when $t = 0$ (here both x and y are assumed to be in euclidean space; to obtain the exact heat kernel over a manifold one needs the eigendecomposition of the LB operator, see (12) below). The parameter t , which represents time in the heat equation (Appendix 2) can be used to obtain the approximation at different scales, with larger t values implying heat has flowed for longer times and the approximate Laplacian is considering larger areas of interest around a given point.

The mesh Laplacian has a simple expression that connects it to the underlying graph Laplacian, as the next remark shows.

Claim 1. For a differentiable function $f(x)$ defined on \mathcal{M} , the discretized approximation of its LB operator (6) results in an $m \times m$ Laplacian matrix acting on vectors f which can be written as:

$$L_{\mathcal{K}}^t = D - W \quad (7)$$

with $W_{ij} = \frac{1}{12\pi t^2} \sum_{T: p_j \in V(T)} A(T) e^{-\|p_i - p_j\|^2/4t}$ for $i = 1, \dots, m$ and $j = 1, \dots, m$ and diagonal matrix D with entries $D_{jj} = \sum_i W_{ij}$.

For a proof, see Appendix 2. The *estimated spectrum* of the LB operator is then given by the eigenvalues of matrix $L_{\mathcal{K}}^t$. Li *et al.* (2015) noted how the mesh Laplacian approximation (6) is a *global* approximation, since computing it at a given point requires the integral over the whole surface \mathcal{M} . Instead, these authors proposed a modification of the mesh Laplacian that uses geodesic distances between points p_i and p_j (as opposed to euclidean distances) and that considers in the last sum only points within a certain radius r of each point x , resulting in the alternative discrete Laplacian approximation:

$$\begin{aligned} L_{\mathcal{K}}^t f(x) &= \frac{1}{4\pi t^2} \int_{y: d(x,y) \leq r} e^{-\frac{d(x,y)^2}{4t}} [f(x) - f(y)] dy \\ &= \frac{1}{4\pi t^2} \sum_{y: d(x,y) \leq r} \frac{A(y)}{3} e^{-\frac{d(x,y)^2}{4t}} [f(x) - f(y)] \end{aligned} \quad (8)$$

where $A(y)$ denotes the area of the one ring neighborhood of point y . By writing the equation above in vector form, it is easy to obtain the Laplacian matrix $L_{\mathcal{K}}^t = D - W$, with $W_{ij} = \frac{1}{12\pi t^2} A(p_j) e^{-d(p_i, p_j)^2/4t}$ for $i = 1, \dots, m$ and $j = 1, \dots, m$ and diagonal matrix D with entries $D_{ii} = \sum_j W_{ij}$. We call this LB approximation the *Localized Mesh Laplacian*. It has the merit of resulting in sparser L matrices, reducing storage and computational requirements, and was used in all the examples and figures shown below.

Remark 1. Relation to the combinatorial graph Laplacian The discrete Mesh Laplacian in equation (6) and the Localized Mesh Laplacian (8), have the same form as the *combinatorial Graph Laplacian* (Chung & Lu, 2006), $L = D - A_{\mathcal{K}}$, where $A_{\mathcal{K}}$ is the adjacency matrix of the mesh \mathcal{K} and D is a diagonal matrix with entries equal to the degree of each vertex. The graph Laplacian is an operator applied to a function defined on the vertices of the graph. It corresponds to the discrete Laplacian if the edge weights are $W_{ij} = 1$, so the discrete LB operator (6) can be thought of as a weighted version of the combinatorial Laplacian where the edge weights are given by the integrated heat kernel (with either euclidean or geodesic distances over the neighborhood of a point, depending on the approximation used) over one third of the area of the one-ring neighborhood of either of its two end points. The graph Laplacian arises when modeling a diffusion process on a network or mesh. Let ψ_i be the amount of some substance at vertex i , and $c(\psi_j - \psi_i)$ be the rate at which the substance flows from vertex j to vertex i , where c is a constant. Then

$$\frac{d\psi_i}{dt} = c \sum_j A_{ij} (\psi_j - \psi_i)$$

where A_{ij} is the i, j element of $A_{\mathcal{K}}$. It is easy to show (Newman, 2010) that

$$\frac{d\psi}{dt} = c(A_{\mathcal{K}} - D)\psi = -cL\psi$$

where ψ is a vector with all ψ_i 's, from which the diffusion equation on a network results: $\frac{d\psi_i}{dt} + cL\psi = 0$, compare to the heat equation in Table 1.

Remark 2. Convergence. Both Belkin *et al.* (2008, 2009) and Li *et al.* (2015) show how as the triangulation \mathcal{K} gets finer, their Laplacians $L_{\mathcal{K}}^t$ (6 and 8) converge pointwise to the continuous LB operator $\Delta_{\mathcal{M}}$ defined on a smooth manifold. Dey *et al.* (2010) further proved the convergence and stability of the spectra of the mesh Laplacian in Belkin *et al.* (2008).

Remark 3. General form of discrete Laplacian approximations. Patané (2017) pointed out that many of the discretized LB operators proposed in the literature can be represented in a unified way as the multiplication of two matrices

$$\tilde{L} = B^{-1}L \quad (9)$$

where B and L are symmetric, positive semi-definite (B is positive definite) matrices and called the mass matrix and the stiffness matrix, respectively. This means \tilde{L} is *symmetrizable* (Liu *et al.*, 2012) and guaranteed to have real eigenvalues. Defining the inner product $\langle x, y \rangle_B = x'By$ we have that $\langle \tilde{L}x, y \rangle_B = x'LB^{-1}By = x'Ly = x'BB^{-1}LY = \langle x, \tilde{L}y \rangle_B$, so \tilde{L} is self-adjoint. We note that although a symmetrizable LB approximation has therefore the desirable property of having real spectrum, not all other desirable properties of their continuous LB operator counterparts can be achieved with a discrete approximation, so there is a “no free lunch” situation, explaining why there are so many discrete approximations proposed to the LB operator, see Wardetzky *et al.* (2007). For instance, the eigenfunctions of the continuous LB operator form an orthogonal basis in $L_2(\mathcal{M})$, however, the eigenvectors of the discrete LB operator approximations $\tilde{L} = B^{-1}L$ do not form an orthogonal basis if using the euclidean inner product, a result of the underlying meshes used for their computation not being uniform on \mathcal{M} (Rustamov, 2007). The non-uniform mesh in turns result in a non-symmetric discrete Laplacian. The eigenvectors of a discrete approximation $\tilde{L} = B^{-1}L$ do form an orthogonal basis but with respect to the B -inner product $\langle \cdot, \cdot \rangle_B$, i.e., $\langle \phi_i, \phi_j \rangle_B = \phi_i' B \phi_j = 0$ for $i \neq j$. For this reason, Rustamov (2007) indicates that only when the mesh is uniform one can expect a discrete Laplacian to be “faithful” to the continuous LB operator. This indicates that mesh pre-processing techniques may be valuable, but we leave this topic for further research.

Proposition 1. The Mesh Laplacian (6) and the Localized Mesh Laplacian (8) can be written as (9) and therefore its eigenvalues are all real.

Proof. From Claim 1, both the Mesh Laplacian and the Localized Mesh Laplacian can be written as:

$$L_{\mathcal{K}}^t = D - W$$

where $W_{ij} = \frac{1}{12\pi t^2} A(p_i, p_j) e^{-\text{dist}(p_i, p_j)^2 / 4t}$ and $D_{jj} = \sum_i W_{ij}$ is diagonal, for $i = 1, \dots, m$ and $j = 1, \dots, m$. The only differences between these two discrete Laplacians are the definitions of area $A(p_i, p_j)$ and distance $\text{dist}(p_i, p_j)$, which are summarized in the following table:

	Mesh Laplacian	Localized Mesh Laplacian
$A(p_i, p_j)$	$A(p_j)$	$\begin{cases} A(p_j) & \text{if } \text{dist}(p_i, p_j) \leq r \\ 0 & \text{if } \text{dist}(p_i, p_j) > r \end{cases}$
$\text{dist}(p_i, p_j)$	Euclidean distance	Geodesic distance

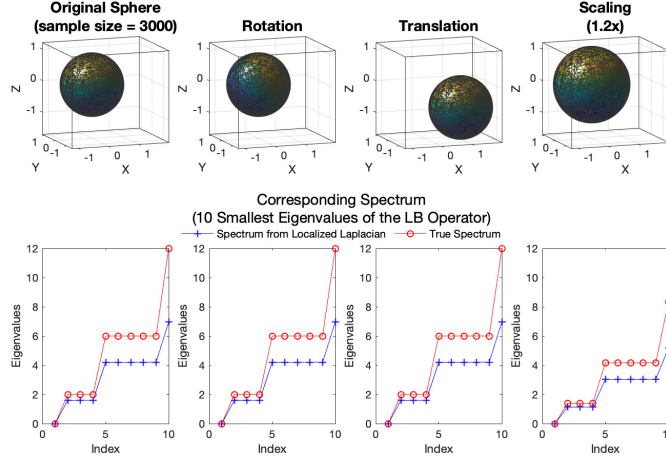


Figure 5: Spectrum of the approximated (discrete) LB operator obtained from a noise-free mesh for different transformations contrasted with the true spectrum of a unit sphere (the localized mesh Laplacian was used in figures 5-8). As can be seen, the true spectrum (in red) is invariant with respect to rigid transformations such as rotations and translations. Scaling the object by s will make the eigenvalues change by $1/s^2$ (here $s = 1.2$ made the eigenvalues decrease close to 30%).

Where recall $A(p_j)$ is the area of the one ring neighborhood of point p_j . Now define a diagonal matrix B where $B_{ii} = A(p_i)$, which is obviously positive definite. Pre-multiplying a matrix by B is the same as multiplying the i th row of the matrix times the i th diagonal element in B , $i = 1, \dots, m$, so matrix BW has elements:

$$(BW)_{ij} = A(p_i)W_{ij} = \frac{1}{12\pi t^2} A(p_i)A(p_i, p_j) e^{-\text{dist}(p_i, p_j)^2 / 4t}$$

It is easy to see that $A(p_i)A(p_i, p_j) = A(p_j)A(p_j, p_i)$ holds with either of the two area definitions above, and indices i and j are interchangeable in both types of distances. Therefore, BW is symmetric for both types of discrete Laplacians. In addition, BD is a diagonal matrix and automatically symmetric. So $BL_{\mathcal{K}}^t = BD - BW = L$ is symmetric, and $L_{\mathcal{K}}^t = B^{-1}L$ is the multiplication of two symmetric, positive semi-definite (B is positive definite) matrices. Therefore, both discrete Laplacians, (6) and (8) are symmetrizable and thus always have real eigenvalues. ■

We have been unable to show how the discrete Laplacian for unstructured cloud points due to Belkin *et al.* (2009) can be written as in (9), so it is not possible to assure if such Laplacian, which we therefore do not use herein, always has a real spectrum. In what follows, we use the Localized Mesh Laplacian due to its sparseness advantage over (6).

The spectrum of the combinatorial graph Laplacian L has some properties with counterparts in the approximated spectrum of $L_{\mathcal{K}}^t$ as the latter is also based on a mesh or network: first, $\lambda_1 = 0$, and the algebraic multiplicity of this eigenvalue gives the number of connected components in the graph. The first eigenvector is constant, and the second eigenvalue λ_2 is greater than zero only if the graph is connected (and only if λ_1 is not repeated). The signs in the second eigenvector, called *Fiedler's vector*, can be used to

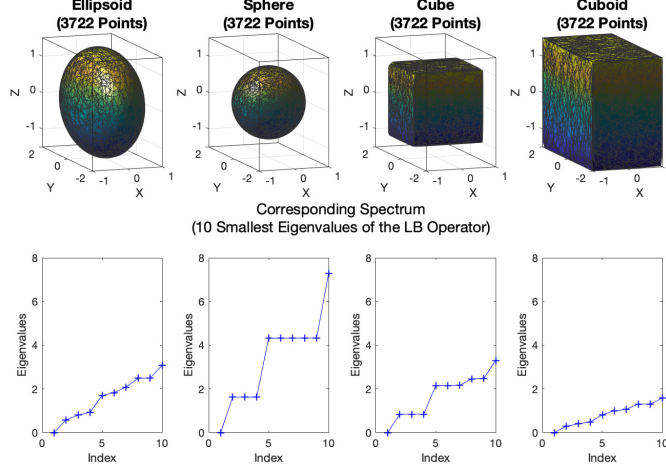


Figure 6: The spectrum of the discrete LB operator contains rich geometric information about the shape of the object. Estimated spectra for different objects obtained from noise-free meshes.

cluster the vertices in two sets, a notion related to the nodal sets of the eigenvector of the LB operator (see Chung & Lu (2006) and also section 7 below).

To demonstrate numerically how the discrete Laplacian approximates the spectrum of a sphere, Figure 5 shows the first 10 eigenvalues of the Localized Mesh Laplacian for a mesh with 3000 points on the unit sphere. Both the true spectrum and the approximation are invariant with respect to rigid transformations (the localized mesh Laplacian (8) was used throughout in this paper).

The spectra of widely different objects are considerably different, as Figure 6 indicates. The quality of the mesh approximation gets better as the mesh size increases, as it can be seen in Figure 7, illustrating numerically the convergence of the estimated LB operator. If the noise is high, the spectrum cannot be estimated well (Figure 8). For moderate levels of noise (which includes both manufacturing errors and measurement errors), we demonstrate in section 4 how the spectrum of the LB operator can still be used for process monitoring purposes.

3.2 Computation and stability of the discrete LB operator spectrum

The computational cost of obtaining the eigenvalues of $L_{\mathcal{K}}^t$ is an $O(m)$ to $O(m^3)$ operation depending on the sparseness of the $m \times m$ matrix. In practice, only the lower part of the spectrum is needed. The Arnoldi algorithm, used in Matlab's function `eigs` to find the first k eigenvalue-eigenvector pairs of a sparse symmetric matrix, has a typical complexity of $O(mk)$. Although not all discrete LB approximations result in a symmetric matrix, many of them are symmetrizable as discussed in Remark 3. It can easily be proved that (λ, ϕ) is an eigenvalue-eigenvector pair of (9) if and only if $(\lambda, B^{1/2}\phi)$ is an eigenvalue-eigenvector pair of matrix $B^{-1/2}LB^{-1/2}$, which is symmetric. Hence, we can gain the extra speed

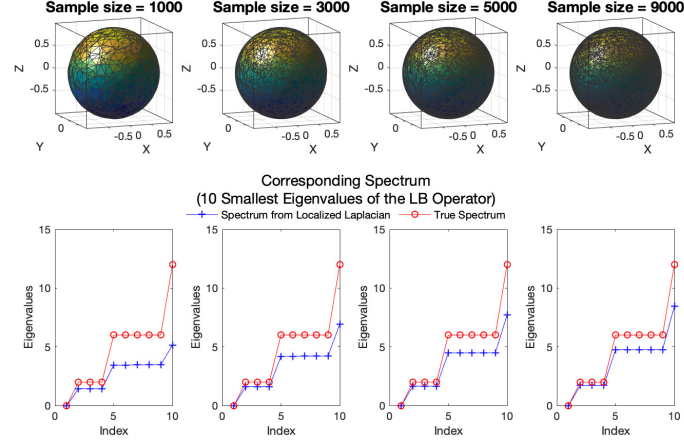


Figure 7: The spectrum of the discrete LB operator converges to the true spectrum as the sample size increases, as proved by Belkin *et al.* (2008) and Li *et al.* (2015)

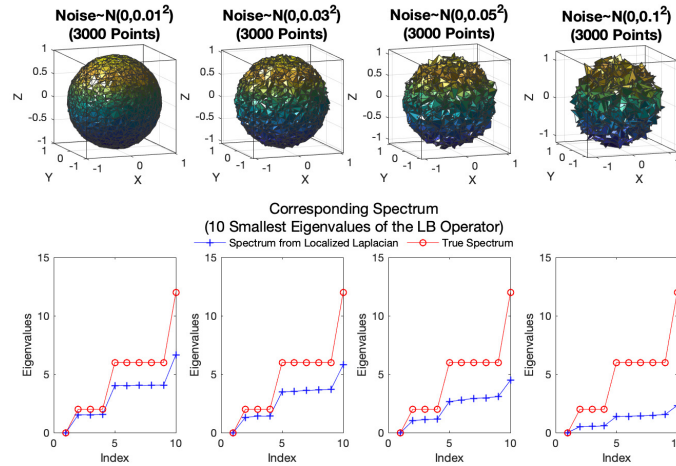


Figure 8: Effect of surface noise on the discrete LB operator (blue) compared to the true spectrum (red) of a noise-free sphere. As the sphere loses its shape due to the severe noise, the spectrum changes.

of the Arnoldi algorithm by finding the eigendecomposition of $B^{-1/2}LB^{-1/2}$ and get the eigenvectors ϕ of \tilde{L} from $B^{1/2}\phi$, which is easy when B is a diagonal matrix as proved in Proposition 1, and this is the computational method we recommend to obtain the spectrum of the discrete LB operators. There are also methods to compute spectral quantities such as heat kernels and diffusion distances (discussed below in section 7) that do not require to compute the LB spectrum first (Patané, 2014).

A numerical question of importance is if the computation of the spectrum of the LB operator is stable or not. Patané (2017) gives the following analysis of the stability of this computation for each single eigenvalue λ . Suppose the estimated Laplacian \tilde{L} is symmetrizable (i.e., it satisfies equation 9) and consider a given single eigenvalue-eigenvector pair λ, ϕ . Perturb $\tilde{L} = B^{-1}L$ by ϵE where E is a disturbance matrix and $\epsilon > 0$ small, and solve for the new eigenvalue-eigenvector pair $\lambda(\epsilon), \phi(\epsilon)$ in $(B^{-1}L + \epsilon E)\phi(\epsilon) = \lambda(\epsilon)\phi(\epsilon)$ with initial conditions (as $\epsilon \rightarrow 0$) $\lambda(0) = \lambda$ and $\phi(0) = \phi$. The magnitude of the derivative $\lambda'(0)$ provides a measure of change of the eigenvalue as L is perturbed. Differentiating with respect to ϵ ,

$$\begin{aligned} \frac{d}{d\epsilon} ((B^{-1}L + \epsilon E)\phi(\epsilon)) &= \frac{d}{d\epsilon} (\lambda(\epsilon)\phi(\epsilon)) \\ B^{-1}L\phi'(\epsilon) + \epsilon E\phi'(\epsilon) + E\phi(\epsilon) &= \lambda(\epsilon)\phi'(\epsilon) + \lambda'(\epsilon)\phi(\epsilon) \end{aligned}$$

Making $\epsilon \rightarrow 0$ we get $L\phi'(0) + BE\phi = \lambda B\phi'(0) + \lambda'(0)B\phi$. Pre-multiplying both sides times ϕ^T , we get $\phi^T BE\phi = \lambda'(0)$ which follows because the B -norm of the eigenvector, $\|\phi\|_B$, is one. Thus, from the Cauchy-Schwarz inequality we have that

$$|\lambda'(0)| = |\phi^T BE\phi| = \langle \phi, E\phi \rangle_B \leq \|E\phi\|_B$$

again, since $\|\phi\|_B = 1$. Thus, the magnitude of change of each eigenvalue is bounded by the B -norm of $E\phi$, and therefore the computation of the eigenvalues with multiplicity one is stable numerically. Furthermore, our numerical experiments show that the lower spectrum is stable with respect to moderate levels of noise, typically encountered in manufacturing. The computation of the spectra is not stable when there are higher multiplicities (Patané, 2017), but as mentioned before, repeated eigenvalues occur due to exact symmetries which will be rare from scanned objects, and our numerical methods did not show evidence of this kind of potential problem.

4 Using the estimated LB spectrum as a tool for SPC

Our proposal is to use the lower part of the Localized Mesh Laplacian spectrum (8), i.e., the spectrum cropped up to certain maximum index, obtained from scanned parts and consider each spectrum a profile from which we derive a general statistical process monitoring technique supplemented by additional post-alarm tools to aid the localization of the defects on a part.

4.1 Permutation tests based on the LB spectrum

Empirical evidence presented by Sun *et al.* (2009b) indicates that commercial 3D scanner noise is not Gaussian. But even for normally distributed, isotropic errors added to a surface, the estimated LB spectra are not multivariate normal. Figure 9 shows the Shapiro-Wilks marginal tests of normality for each of the first 500 eigenvalues of 200 “acceptable” parts simulated based on the CAD model triangulation in Figure 10 below to which we added isotropic $N(0, \sigma^2 \mathbf{I}_3)$ measurement noise. It is therefore necessary to develop distribution-free process monitoring methods for the LB spectrum.

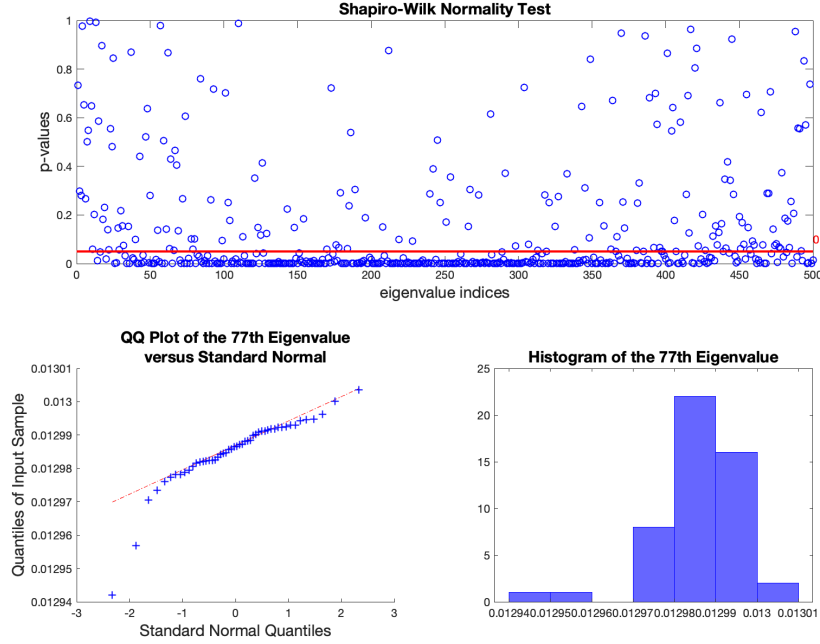


Figure 9: Top: p-values of the Shapiro-Wilks test of normality for the first 500 eigenvalues from 200 realization of the CAD model in figure 10 with normally distributed noise in each coordinate/vertex. Bottom: QQ plot and histogram for the distribution of the simulated 77th eigenvalue. The spectra is not normally distributed even if the noise is normal.

To obtain an initial assessment of the detection capabilities of the spectrum of the LB operator, we use 2-sample permutation tests to compare the mean LB spectra between two groups of parts using a component-wise Wilcoxon rank test. Represent the spectra of the estimated LB operator (sorted from smallest to largest, up to some given index p) of each part i by $\mathbf{X}_i \in \mathbb{R}^p$, and let the two samples be $\{\mathbf{X}_1, \dots, \mathbf{X}_m\} \sim F(\boldsymbol{\mu}_0)$, when the process is in control or acceptable, and $\{\mathbf{X}_{m+1}, \dots, \mathbf{X}_{m+n}\} \sim F(\boldsymbol{\mu}_1)$ for parts that have an out of control condition. Given the non-normality of the spectrum data, in our preliminary tests we use a nonparametric, distribution free permutation test for $H_0 : \boldsymbol{\mu}_0 = \boldsymbol{\mu}_1$ using two different types of statistics: the maximum t-statistic (Reuter *et al.* , 2007) and the componentwise Wilcoxon rank sum statistics (Chen *et al.* , 2016). The maximum t-statistic is defined as

$$t_{\max} = \max_{1 \leq j \leq p} \frac{|\sum_{i=1}^m X_i(j)/m - \sum_{i=1}^n X_{m+i}(j)/n|}{SE_j} \quad (10)$$

Here $X_i(j)$ is the j th element of X_i (in our case, the j th eigenvalue of part i), and SE_j is the pooled standard error estimate of the j th eigenvalue

$$SE_j = \frac{\sqrt{(m-1)\sigma_{1,m,j}^2 + (n-1)\sigma_{m+1,m+n,j}^2}}{\sqrt{\frac{1}{m} + \frac{1}{n}}}$$

where $\sigma_{i,k,j}$ is the standard deviation of the j th element in sample $\{\mathbf{X}_i, \mathbf{X}_{i+1}, \dots, \mathbf{X}_k\}$.

For specifying the componentwise Wilcoxon rank sum statistic, denote the rank of the j th eigenvalue from the i th part, with respect of the pool of $m+n$ parts, as R_{ji} ($i = 1, \dots, m+n$ and $j = 1, \dots, p$) and define:

$$T_j = \frac{\sum_{i=1}^m R_{ji} - E[\sum_{i=1}^m R_{ji}]}{\sqrt{\text{Var}(\sum_{i=1}^m R_{ji})}}, \quad j = 1, \dots, p$$

where $\sum_{i=1}^m E[R_{ij}] = m(m+n+1)/2$ and $\text{Var}(\sum_{i=1}^m R_{ij}) = mn(m+n+1)/12$. The test statistic is formed by combining the T_j using $T_0 = \sum_{j=1}^p T_j^2$, with a large value of the test statistic leading to rejection of H_0 .

Both statistics t_{\max} and T_0 are intuitive, as there is no explicit mapping available from the eigenvalues of the LB operator to the manifold \mathcal{M} , and differences in *all* the first p eigenvalues should be considered jointly as evidence of a difference between the two objects.

Figure 10 shows the results of permutation tests between two samples. The first sample (with sample size 10) is a group of acceptable parts, while the second sample (with sample size 5) is a group of parts of the type shown on top of each column, where the first three parts have different types of defects (chipped corners or a protrusion) while the last one is acceptable in the sense of being equal the CAD design of the part plus isotropic white noise. To make the simulated data realistic, each part has a different number of points (between 26750 and 26850 points) since real datasets from a non-contact sensor will not have identical number of points/part. We added isotropic $N \sim (0, 0.05^2 \mathbf{I}_3)$ noise to all points of all part types. The second row of plots in the figure are results from the permutation test results using the maximum t-statistic, while the last row is using the Wilcoxon rank-sum statistic $T_0 = \sum_j T_j^2$ with T_j as in (4.1), both using $p = 500$. In each of the small figures showing the test results, the blue bars are the empirical pdf's of the test statistic from all permutations, while the red line indicates the observed value of the test statistic T_0 . Both the maximum-t and rank-sum tests are one-sided. The red numbers under the red lines are the estimated p-values for the corresponding tests, defined as the number of observations with more extreme (larger) value than T_0 divided by the total number of permutations (3003 for sample sizes 10 and 5, note this is an exact permutation test).

We repeated the experiments in figure 10 using eigenvalues normalized by area, given that from (5) they relate inversely to the surface area of \mathcal{M} . For small, localized defects on the surface of a part, the detection capabilities of the LB spectrum using either normalized or non-normalized are very similar, and therefore the normalized spectrum results are not

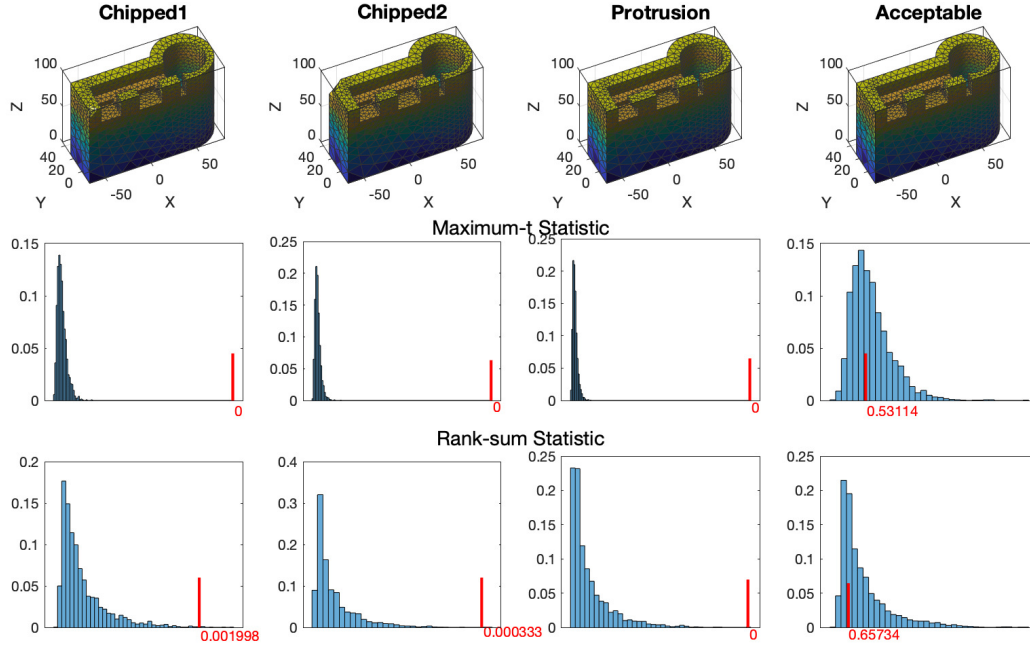


Figure 10: Permutation tests based on the statistics t_{\max} (second row of plots) and the rank-sum statistic $T_0 = \sum T_j^2$ (bottom row) for the difference between two groups of parts, using unnormalized eigenvalues. A sample of 5 parts of the type depicted at the top of each column was compared against a sample of size 10 of the acceptable part on the last column. The first three parts contain different types of defects. All simulated parts have isotropic $N(0, 0.05^2 \mathbf{I}_3)$ noise added to each vertex and parts have meshes with different number of points ranging between 26750 to 26850. The three types of defects result in strong rejections of H_0 (small p-values) whereas comparing acceptable vs. acceptable parts leads to failure to reject. Numbers in red are the empirical p-values based on all 3003 permutations.

shown here. Since we wish to detect changes in shape and in size, and not only in size, we suggest using the *unnormalized* spectrum, which will be used in the following sections.

Figure 11 shows the distributions of the permuted test statistics, with the small subplots showing the empirical distributions of the estimated p-values (as defined above) when the permutation test procedure is repeated 1000 times. In these figures, the last column of plots shows the case when both groups of parts consist of acceptable parts, i.e., the null hypothesis is true. As it is easy to show, in such case the theoretical p-value should follow a standard uniform distribution, and this is approximately the case in the depicted histograms of p-values. In the other cases, when we are testing defective parts against acceptable parts, it is desired to have p-values very close to zero, as it is indeed the case.

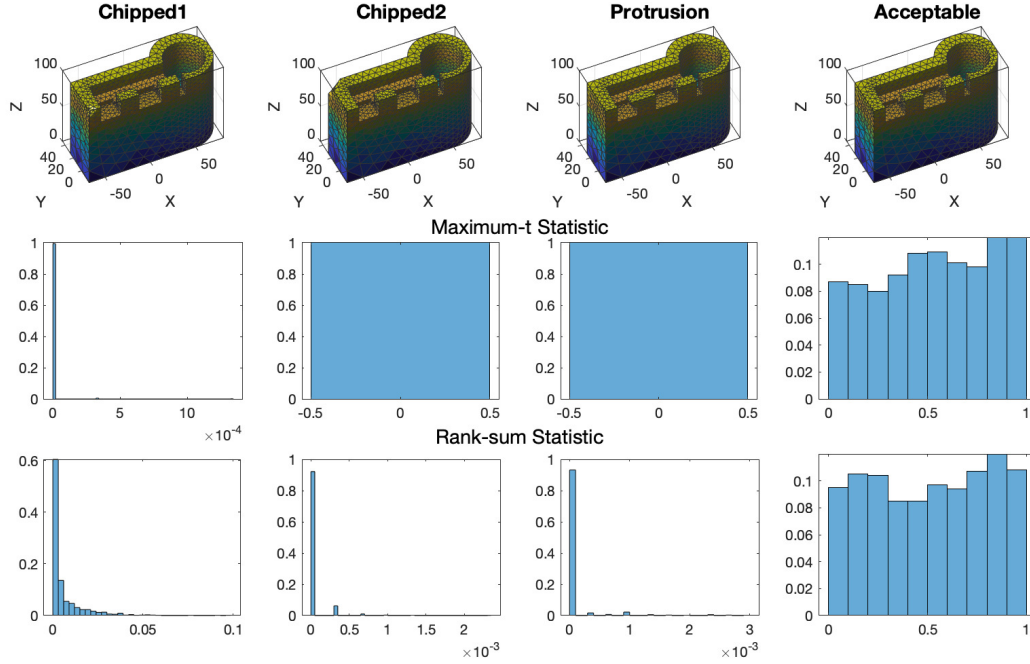


Figure 11: P-value distributions of the permutation tests of Figure 10 based on the unnormalized eigenvalues. A single “thick bar” indicates all values were zero. Note how the acceptable vs. acceptable comparison on the last column results in a near-uniform distribution of p-values, as expected.

These comparisons indicate the potential for using the LB spectrum and permutation tests for shape difference detection. These are not however, an SPC scheme, since for on-line, “Phase II” monitoring we require a sequential test, as further discussed below.

4.2 On-line SPC scheme (“Phase II”)

Given the non-normality of the LB spectrum, for on line statistical control we recommend to use a multivariate permutation-based control chart. We have used, with some modifications as discussed below, Chen *et al.* (2016) distribution-free multivariate exponentially-

weighted moving average (“DFEWMA”) chart, and applied it to the lower part of the estimated LB spectra. Consider the set of the j th component of the vectors one wishes to monitor (eigenvalues of the LB spectra, in our case), taken from observation k to the most recent observation n , $\mathcal{X}_{k,j}^n = \{X_{jk}, \dots, X_{jn}\}$. Let R_{jni} be the rank of X_{ji} among $\mathcal{X}_{-m_0+1,j}^n$, where m_0 is the number of observed vectors in the in-control (IC) state (usually from a “phase I” SPC step). We wish to test the equality of the location of the samples $\mathcal{X}_{-m_0+1,j}^{n-w}$ and $\mathcal{X}_{n-w+1,j}^n$, that is, the in-control observations compared to the most recent observations in a “window” of w observations.

The idea of the DFEWMA chart is to compute the “exponentially weighted” rank statistic $(1 - \lambda)^{n-1} R_{jni}$ of the last w observations among all IC observations thus far. If these ranks are extreme (large or small) this is evidence the process has changed from its IC state. The exponential weights give more weight to the more recent observations within the last w and can be useful to detect smaller process changes. We therefore use the statistic:

$$T_{jn}(w, \lambda) = \frac{\sum_{i=n-w+1}^n (1 - \lambda)^{n-i} R_{jni} - E \left[\sum_{i=n-w+1}^n (1 - \lambda)^{n-i} R_{jni} \right]}{\sqrt{\text{Var} \left(\sum_{i=n-w+1}^n (1 - \lambda)^{n-i} R_{jni} \right)}} \quad (11)$$

For given m_0 in-control observations and a false alarm probability α determining the geometric distributed in-control run lengths (hence the IC average run length is $1/\alpha$), the remaining chart design parameters are thus the weight λ and the window size w . In Appendix 3 we derive the following moment expressions, which consider the covariances of the weighted ranks in the sum:

$$E \left[\sum_{i=n-w+1}^n (1 - \lambda)^{n-i} R_{jni} \right] = \frac{1 - (1 - \lambda)^w}{\lambda} \frac{m_0 + n + 1}{2}$$

and

$$\text{Var} \left(\sum_{i=n-w+1}^n (1 - \lambda)^{n-i} R_{jni} \right) = \begin{cases} \frac{w(m_0+n+1)(m_0+n-w)}{12} & \lambda = 0 \\ \frac{1 - (1 - \lambda)^{2w}}{2\lambda - \lambda^2} \frac{(m_0+n+1)(m_0+n-1)}{12} - \left(\frac{1 - \lambda - (1 - \lambda)^w}{\lambda^2} - \frac{(1 - \lambda)^2 - (1 - \lambda)^{2w}}{\lambda^2(2 - \lambda)} \right) \frac{m_0+n+1}{6} & \lambda \neq 0 \end{cases}$$

We note these expressions are not the same as in Chen *et al.* (2016), who weighted the standardized ranks (4.1) rather than standardizing the weighted ranks as we do (there are some errors in their formula even for their weighted standardized ranks, see Appendix 3). A sequential test statistic based on $T_{jn}(w, \lambda)$ statistics is the sum of squares $T_n(w, \lambda) = \sum_{j=1}^p T_{jn}^2(w, \lambda)$, used by Chen *et al.* (2016) (maximum statistics could also be used instead). Here we report results based on $T_n(w, \lambda)$ and the moment expressions above.

To illustrate the use of the resulting permutation chart, we simulated again parts from the CAD part model shown in Figure 10. Mesh sizes varied randomly (in the range 26750 to 26849 vertices). Simulations were comprised of a “Phase I” of 50 in-control (nominal plus noise), followed by an on-line “Phase II” where defectives (parts with a protrusion

in one of its “teeth”, see Figures 10-11, third column) were introduced starting at part no. 21. Figure 12 shows simulations of the modified DFEWMA charts under different parameters λ and α . The chart has a variable control limit that depends on the observed realization of the underlying process, thanks to which it has a geometric in-control run length distribution (the main results in Chen *et al.* (2016) hold as well under the different test statistic (11) we use). In every case, detection of the out of control (OC) state occurred within the first 3 observations.

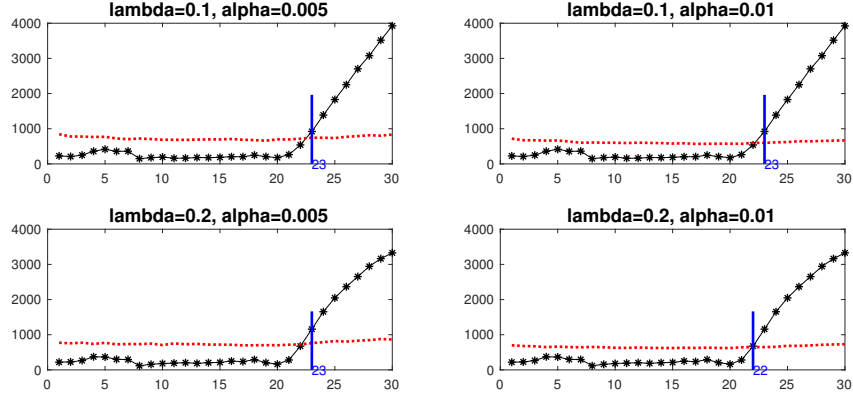


Figure 12: DFEWMA charts applied for “Phase II” of a process producing the same part as depicted in previous figures. Fifty in-control parts (with a random number of meshes and noisy vertex coordinates) were simulated, after which the DFEWMA chart was used for on-line control. As it can be seen, the LB spectrum quickly detects the change in the process producing the parts.

4.3 Run length behavior

To gain a more complete sense of the effectivity of the SPC chart, we conducted a run length analysis based on simulation of cylindrical parts of increasingly more deformed shape, with parts acquiring a more “barrel-like” shape as an OC parameter is modified, to allow us to compute out of control run lengths parametrized in a simple way. We also conducted a run length analysis simulating realizations of the part (and its defect types) shown in Figure 10. Given that a run length analysis implies computation of thousands of LB spectra, to avoid long computation times, we used smaller mesh sizes, with 1995 \sim 2005 points for the cylindrical parts and 1675 \sim 1680 points for the parts in Figure 10. We also permuted the already simulated parts instead of simulating new parts for new replications to further reduce the computational cost while keeping the variability of the run lengths in our analysis.

We applied the DFEWMA charts –with the moments as described in section 4.2– to the LB spectrum with $p = 200$ and also applied it to the optimal function value returned by the ICP algorithm (2), which is a measure of the difference between two configuration matrices after discounting similarity transformations. Table 2 shows the average run lengths (ARL) and the standard deviation of the run lengths (SDRL) in the in-control processes, where we use both a perfect cylinder with radius 10 and height 50 and the acceptable part in the last column of Figure 10, both with isotropic $N(0, 0.05^2 \mathbf{I}_3)$ noise added. As the table shows, all

	LB spectrum		ICP measure	
	ARL	SDRL	ARL	SDRL
Geometric Distribution	20	19.49	20	19.49
In-control cylinder	20.8465	20.6978	20.4240	19.8066
In-control part	20.3841	19.6678	20.5730	19.9226

Table 2: In-control run length performance of the DFEWMA charts applied to the LB spectrum and ICP objective. Results are obtained from 10,000 replications. Chart parameters were set at $m_0 = 50, w = 5, \lambda = 0.1$, and $\alpha = 0.05$ which corresponds to a geometric in-control ARL of 20. Results for both a cylinder and for the part in figure 10, both equal to the CAD model plus isotropic noise $N(0, 0.05^2 \mathbf{I}_3)$.

run lengths have nearly geometrical behaviors, which is consistent with the theorem given in Chen *et al.* (2016).

For the out-of-control analysis of the cylindrical parts, we added a first harmonic with amplitude δ times the standard deviation of the noise to the radius, so the deformed radius at height h becomes $10 + 0.05\delta \sin(h\pi/50)$, adding also isotropic $N(0, 0.05^2 \mathbf{I}_3)$ noise to the points. Table 3 compares the ARL and SDRL of both methods (LB spectrum and ICP) as a function of the OC parameter δ . The LB spectrum is very sensitive to changes in the shape of an object, having almost immediate detection of the deformation of the cylinder for $\delta \geq 0.005$ (an ARL of around 3 means that the chart signals as soon as the majority of the parts in the window of size w are defective). On the other hand, the ICP measure is less efficient than the LB spectrum, especially when δ is very small (note also the large SDRL values). This is because the small increase in the ICP statistic caused by a slight deformation can be masked by the natural variability of the in-control process, plus the inherent variability in the ICP algorithm itself (recall that (2) is a hard non-convex combinatorial problem), making it hard for the chart to distinguish the change to an OC condition until more parts are available. However, this would not be a problem for the LB spectrum because it is reflecting the overall shape of the parts. Both DFEWMA charts have a limiting ARL, because as mentioned by Chen *et al.* (2016) these are rank-based charts which are more effective at detecting small changes in a process, with the ranks not changing much after further increases in the size of the process change introduced. These authors recommend their chart when the ratio m_0/p is small, which are ideal conditions for high quality discrete manufacturing processes, hence we show most of our run length results for $m_0/p = 50/200$. The limiting ARL value depends on a complicated form in the in-control and out of control states and on the chart parameters $(m_0, \lambda, \alpha, w, p)$.

We also conducted the OC run length analysis for the part and defects shown in Figure 10, where we consider three types of defects corresponding to the first three columns in the figure. The ARLs and SDRLs for both methods (LB spectrum and ICP) for the three defective parts are summarized in Table 4. In this case, the ICP method works consistently better than the LB spectrum to detect all three types of defective parts. This is because the three defects are very localized and evident to the eye, making the increase in the ICP objective function quite significant. As these three defect types are local *and the mesh size used is very small*, they do not change the overall shape of the part enough for the LB spectrum to quickly detect the changes in the process, particularly with the chipped part

	LB spectrum		ICP measure	
	ARL	SDRL	ARL	SDRL
$\delta = 0.0005$	19.0055	52.3627	140.7616	174.9843
$\delta = 0.005$	3.0654	0.7361	102.0958	147.0925
$\delta = 0.5$	3.0706	0.7422	92.1004	145.4446
$\delta = 1$	3.0668	0.7405	8.5135	12.5958
$\delta = 2$	3.0623	0.7399	3.6150	0.8464
$\delta = 3$	3.0705	0.7442	3.5675	0.8438
$\delta = 10$	3.0572	0.7340	3.5856	0.8260

Table 3: Out of control run length performance of the DFEWMA charts applied to the LB spectrum and ICP measure with cylindrical parts. Results are obtained from 10,000 replications, each with 50 IC cylinders followed by a sequence of defective cylinders until detection in “Phase II”. Chart parameters used are: $m_0 = 50, w = 5, \lambda = 0.1$ and $\alpha = 0.005$, which corresponds to a geometric in-control ARL of 200.

Defect type	LB spectrum		ICP measure	
	ARL	SDRL	ARL	SDRL
Chipped #1	205.8060	208.3037	3.5956	0.8140
Chipped # 2	84.8106	149.6862	3.5922	0.8365
Protrusion	4.1782	1.1185	3.5907	0.8324

Table 4: Out-of-control run length performance of the DFEWMA charts applied to the LB spectrum and ICP objective with parts shown in Figure 10. Results are obtained from 10,000 replications, each with 50 IC parts followed by a sequence of defective parts until detection in “Phase II”. The parameters used for the charts are: $m_0 = 50, w = 5, \lambda = 0.1, \alpha = 0.005$ which corresponds to a geometric in-control ARL of 200. Mesh sizes were necessary small (1675 to 1680), and the spectrum chart is unable to quickly detect the smaller defects (chipped type 1 and 2), a problem that disappears when larger meshes are used, see text.

#1, which is the smallest and more localized type of defect, with a faster detection for the protrusion defect part, which is the largest of the 3 defects relative to the mesh. To demonstrate that with larger meshes the LB spectrum would detect these types of defects quicker, consider Figure 10 where we have large meshes, and the p-values of the same Wilcoxon rank-sum tests (bottom row) are significant for all three cases. This indicates that the chart will signal faster with larger mesh sizes. We also note that chipped defect #1 has a slightly larger p-value in Figure 10, and in Figure 11 the distribution of its p-values has a thicker right tale than for the chipped #2 and protrusion defects. This shows the chipped #1 defect is harder to detected by nature and explains why it results in the longest run lengths, essentially becoming undistinguishable from the IC operation of parts if using a small mesh size.

5 Post alarm diagnostics

We have proposed a multivariate permutation SPC chart on the lower spectrum of the LB operator as a tool to detect *general* out of control (OC) states in the process that are not precisely defined, similarly to the role standard Shewhart charts have, as described by Box & Ramírez (1992). Once an alarm is triggered, an investigation of the *specific* assignable cause that is normally carried out should include the *localization* of the defect on the part surface or manifold \mathcal{M} , a task we now describe.

Suppose we have a part that has triggered an alarm in the SPC charts described above and we have also have available a CAD model for the part being produced. In order to localize the defect on each part, we apply the ICP algorithm to register the CAD model and the part that triggered the alarm (we use the ICP algorithm implemented by P. Bergstrom and available in Matlab Central). Upon completion, the ICP algorithm provides for each point on the defective part the index of the closest point on the noise-free CAD model, so that *deviations from target* can be computed as the Euclidean distance between them (this is the minimum distance $\min_{j=1,\dots,m_2} C(\Gamma \mathbf{x}_{q,i} + \gamma, \mathbf{x}_{p,j}) = \min_{j=1,\dots,m_2} \|\Gamma \mathbf{x}_{q,i} + \gamma - \mathbf{x}_{p,j}\|$ in problem (2), with \mathbf{X}_q and \mathbf{X}_p being the OC part and the CAD model respectively).

Figure 13 shows three different locally defective parts, each with different number of points and with isotropic errors $N \sim (0, 0.05^2)$ added to all three coordinates. We color each point on the OC part proportionally to these deviations, with lighter colors corresponding to larger deviations. As it can be seen, the location of each of the 3 defects on a part, the two parts with chipped corners and the part with a protrusion in one of its “teeth”, is very accurately identified. We suggest to conduct this ICP localization diagnostic after each SPC alarm.

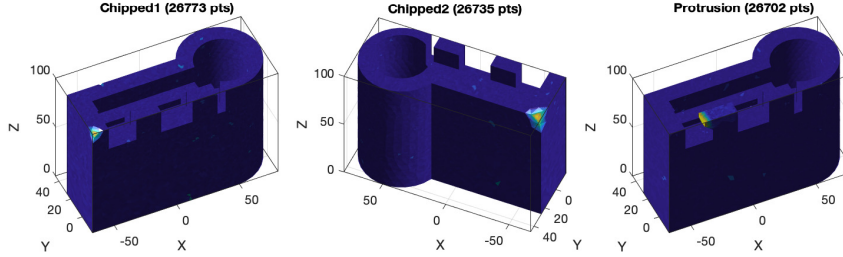


Figure 13: ICP post-alarm diagnostic to localize the occurrence of a defect on the surface of a part. Lighter areas indicate greater deviations from the nominal (CAD) model.

When a global change in shape occurs due to an out of control condition, the ICP localization diagnostic will not work as well as in the case of very localized defects unless the change of shape is very evident. To illustrate, Figure 14 shows three out-of-control cylindrical parts with increasing δ values. The number of points varies from part to part and the same isotropic noise we have been using is added. Each part is color coded by the deviation from CAD target and lighter colors means larger deviations. The global deformation of the cylinders is strongest along the “waist” of the cylinder, and is only detectable by the ICP registration when δ is large enough to be quite evident to the eye.

This is consistent with our findings in the OC run length analysis, where the ICP measure is more effective with relatively larger δ values. A similar "defect localization" could be performed with a registration method based on other distance functions between points, such as spectral distances, see section 7.

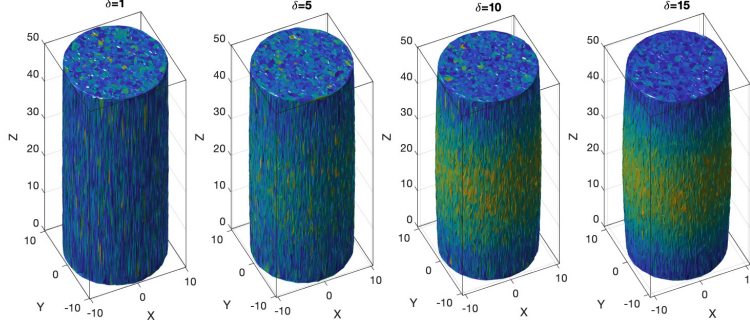


Figure 14: ICP post-alarm diagnostic to localize the occurrence of a defect on the surface of a part. Lighter areas indicate greater deviations from the nominal (CAD) model.

6 A permutation-based SPC scheme for “Phase I”

For the startup or “phase I” of a statistical process control scheme, we suggest using the distribution-free multivariate chart proposed by Capizzi & Masarotto (2017), available in their R package **dfphase1**, applied to the spectrum of the LB operator. Similar to the DFEWMA chart, these authors used rank related statistics, so their method is more sensitive to small rather than large changes in the process. We point out that this multivariate chart requires the number of variables to be strictly smaller than the total number of observations (parts) available in “Phase I”. This condition does not hold for the lower part of the LB spectrum, since the number of eigenvalues (usually several hundreds) is typically larger than the number of “Phase I” observations (usually no larger than 100. We fix it to 50 to be consistent with our “Phase II” analysis). To deal with this situation, we recommend performing a principal component analysis (PCA) first to reduce the dimensionality of the “Phase I” spectral data. Following Capizzi & Masarotto (2017), the performance of the chart is evaluated based on the false alarm probability (FAP) for both in-control and out-of-control scenarios.

Given the “Phase I” dataset consisting of the cropped spectra, we first discard the first eigenvalue of each part because it is theoretically zero (non-zero first eigenvalues from the estimated LB operator are pure numerical error). Next we scale all other eigenvalues such that they have unit variance and thus receive the same weight for PCA. Finally, PCA is performed and the first few principal components are the variables used in the “Phase I” chart. We compare the performance of four different numbers of principal components (PCs): the first PC, the first 10 PCs, the first 25 PCs, and the first 49 PCs. We also consider using the first 49 eigenvalues (i.e. the second to the fiftieth eigenvalue after discarding the

	1st PC	first 10 PCs	first 25 PCs	first 49 PCs	first 49 eigenvalues
Noise-free cylinder	0.0522	0.0557	0.0531	0.0507	0.0512
Acceptable part	0.0544	0.0488	0.0548	0.0526	0.0525

Table 5: In-control false alarm probability (FAP) of the “Phase I” scheme by Capizzi & Masarotto (2017) with different number and types of variables derived from the lower part of the LB spectrum. The nominal FAP is $\alpha = 0.05$. Results are obtained from 10000 replications. All parameters are at their default values as in the R package **dfphase1**.

first one) as a benchmark to evaluate the benefit of using PCA. The same part type as in section 4.3 is used here so the dimensionality of the lower spectra is still 200.

Table 5 summarizes the in-control false alarm probability (FAP), where similarly to Section 4.3, we sampled and permuted 50 IC parts from pre-simulated 40,000 IC parts instead of simulating new parts for new replications to reduce the computational effort. As the table shows, all cases have a FAP close to the nominal $\alpha = 0.05$, indicating the method works well either with or without PCA.

The out-of-control false alarm probabilities for the cylindrical parts with increasing δ values are shown in table 6. Each replication consists of 25 simulated IC parts followed by 25 simulated OC parts under the same isotropic noise as before ($N(0, 0.05^2 \mathbf{I}_3)$). The table indicates that the cropped spectrum (first 49 eigenvalues) does not have any detection power as its alarm probabilities are always small and close to α . This is expected as we lose the information contained in the larger eigenvalues when we crop the spectrum. Another important observation is that using fewer principal components works much better than more principal components, with using only the first PC of the cropped spectrum working best. This can be explained by the hierarchical structure of the principal components, i.e., the PCs are more likely to be noise as their index increases. For example, the first 10 principal components already account for more than 95% of total variance, so the more principal components we included, the more noise is entering into the test statistics. We point out how the percentage of variance explained by the first 10 principal components increases as the out of control parameter δ increases, so it is safe to only use the first several principal components.

The OC alarm probabilities for the defective parts shown in figure 10 are shown in Table 7. Each new set of “phase 1” data consists of 25 simulated IC parts and 25 simulated OC parts with the same isotropic noise level as before. As it can be seen, the protrusion defect is the easiest to detect, followed by chipped #2 defect, with the chipped #1 type of defect being the hardest to detect. This is consistent with our OC results from “phase II” (table 4). Similarly to the cylindrical parts, the first 49 eigenvalues do not have any detection power and the first 49 PCs are too noisy. Again, using 10 and 25 PCs provides satisfactory alarm probabilities, as they account for 70% and 90% of the total variance in the “phase 1” dataset, respectively. In practice, we recommend using a scree plot to decide the best number of principal components to use.

	1st PC	first 10 PCs	first 25 PCs	first 49 PCs	first 49 eigenvalues
$\delta = 0.0005$	0.8601	0.4681	0.2085	0.0486	0.0535
$\delta = 0.005$	1	1	1	0.0615	0.0577
$\delta = 0.5$	1	1	1	0.0239	0.0557
$\delta = 1$	1	1	1	0.0038	0.0468
$\delta = 2$	1	1	1	0.0004	0.0472
$\delta = 3$	1	1	1	0	0.0510
$\delta = 10$	1	1	1	0	0.0515

Table 6: Out-of-control alarm probability of the “Phase I” scheme by Capizzi & Masarotto (2017) for the cylindrical parts with increasing out-of-control parameter δ . Different number and types of variables were investigated. The IC nominal FAP is $\alpha = 0.05$. Results are obtained from 10000 replications. All default parameters in Rpackage **dfphase1** were used.

Defect type	1st PC	first 10 PCs	first 25 PCs	first 49 PCs	first 49 eigenvalues
Chipped #1	0.0549	0.1137	0.1913	0.049	0.0483
Chipped #2	0.5509	0.9961	1.0	0.0747	0.051
Protrusion	0.4247	1.0	1.0	0.0844	0.0471

Table 7: Out-of-control alarm probabilities of the “Phase I” SPC scheme by Capizzi & Masarotto (2017) for the part defects in figure 10. Different number and types of variables were investigated. The nominal in-control FAP is $\alpha = 0.05$. Results obtained from 10000 replications. All default parameters in Rpackage **dfphase1** were used.

7 Discussion: other intrinsic geometrical statistics for process control

7.1 Heat kernel and diffusion distances

For a long time, researchers in computer vision have aimed at finding descriptors of shapes for object recognition that would use properties of a cloud of points from the point of view of each point. In a highly cited paper, Belongie *et al.* (2002) introduce the concept of a *shape context*, a local description of the shape in the vicinity of a given point, and use it for registration of objects. The main idea is to measure the frequency and location of other points in the neighborhood of each point of a shape and use these measures as costs to be minimized in a classical weighted matching problem (thus points with similar local information tend to be matched), solvable via Linear Programming. For a point i in an object, Belongie et al. propose to compute a 2-dimensional histogram where the number of points nearby are counted. If r is the Euclidean distance between two points of the shape, the 2-dimensional histogram $h_i(\cdot, \cdot)$ extends along $\log r$ and θ , measuring the distance and direction where the nearby points are located. The 2-dimensional histogram formed by the frequencies $h_i(\cdot, \cdot)$ is called the “context” of point i by these authors and was computed for recognition of 2-dimensional shapes via registration. Extending this concept to 3D objects is harder as higher dimensional “histograms” need to be computed at each point to locally describe the points in a neighborhood of a given point. In contrast, the lower part of the spectrum of the LB operator provides a *global* description of the shape, with more detail included in higher eigenvalue-eigenvector pairs. As discussed, the LB operator results from the solution of the Helmholtz equation, which relates to the spatial part of the heat equation. It is thus reasonable to look at the *temporal* solution of the heat equation to try to find additional *local* intrinsic descriptors of the geometry of an object.

A result due to Huber (see e.g., Buser (1992)) proves how two Riemannian surfaces have the same sequence of eigenvalues of their LB operator if and only if they have the same sequence of lengths of their closed geodesics, thus, in principle, the geodesics, evidently intrinsic, could be used for detecting part to part differences in a SPC scheme. For our prototypical part, Figure 15 illustrates some geodesics between a point and some others in the part under consideration, as well as the geodesic distance between the point and all others on the mesh defining the part. Geodesics, being intrinsic to the surface, are simpler to compute than the spectrum, but in practice, the question, if one wishes to apply Huber’s theorem, is that geodesics are greatly affected by noise (Lee & Wasserman, 2010) and it is not clear how many geodesics distances are needed to compare between 2 objects, a manufactured/scanned one, and a noise-free CAD model, in order to find local defects on the surface of the manufactured part. In this section, we report our experiments with geodesic distances and other more robust intrinsic distance functions based on the heat kernel defined on the surface of a part.

Given the spectrum $\{\lambda_i\}$ and associated eigenfunctions $\{\phi_i(\cdot)\}$ of the LB operator on \mathcal{M} , the *heat kernel* on a manifold $\mathcal{M} \in \mathbb{R}^n$ is a bilinear function $k_t(x, y) : \mathbb{R}^+ \times \mathcal{M} \times \mathcal{M} \rightarrow \mathbb{R}$,

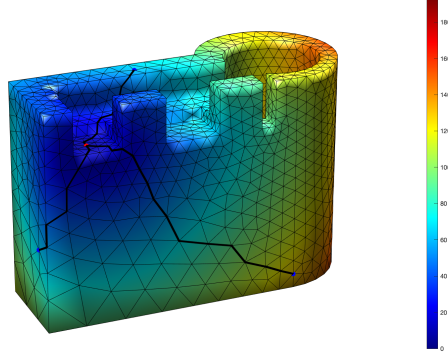


Figure 15: Illustration of geodesics and geodesic distances on a mesh (triangulation) of a noise-free part: darker lines are the geodesics between a point and three other points on the triangulation (mesh) of our prototypical part. Color corresponds to geodesic distance from the first point over the triangulation, with redder colors indicating longer distances.

given by the decomposition:

$$k_t(x, y) = \sum_{i=0}^{\infty} e^{-\lambda_i t} \phi_i(x) \phi_i(y) \quad (12)$$

which can be thought of as the amount of heat transmitted from x to y in time t if there is a unit heat source at x at $t = 0$. The heat kernel satisfies the heat equation, i.e., $\partial k_t(x, y) / \partial t = \Delta k_t(x, y)$. For small values of t , $k_t(x, y)$ reflects *local properties* of \mathcal{M} around x ; for larger values of t it reflects the *global structure* of \mathcal{M} from the point of view of x . It is, in a sense, conveying analogous information as Belongie *et al.* (2002) “shape contexts”. There is a close relationship between the heat kernel and geodesic distances $g(x, y)$ for $x, y \in \mathcal{M}$:

$$-g(x, y)^2 = \lim_{t \rightarrow 0} 4t \log k_t(x, y)$$

(see Sun *et al.* (2009a)), which can be shown directly by taking the limit to $k_t(x, y) \approx \frac{1}{4\pi t} e^{-g(x, y)^2 / (4t)}$ which is an approximation of (12) for small t .

The heat kernel can be interpreted as the transition density function of a Brownian motion on \mathcal{M} (Sun *et al.*, 2009a), or alternatively, the estimated heat kernel, using a discrete LB approximation based on a mesh, can be related to the transition probabilities of a random walk process defined on the mesh, a property used in computer graphics by some authors (see, e.g., Sinha & Ramani (2014)) for shape similarity assessment.

Sun *et al.* (2009a) propose to use the “autodiffusion” $k_t(x, x)$ at different points on a mesh as a “Heat kernel Signature” used to identify shapes of objects. A useful notion related to the heat kernel is the *diffusion distance* between $x, y \in \mathcal{M}$ defined by the interplay of heat from x to y and from y to x :

$$d_t^2(x, y) = k_t(x, x) + k_t(y, y) - 2k_t(x, y) = \sum_i e^{-\lambda_i t} (\phi_i(x) - \phi_i(y))^2 \quad (13)$$

The diffusion distances are intrinsic and more robust to changes in the mesh as they are an “average” distance over all possible paths between two points on the mesh, and are not

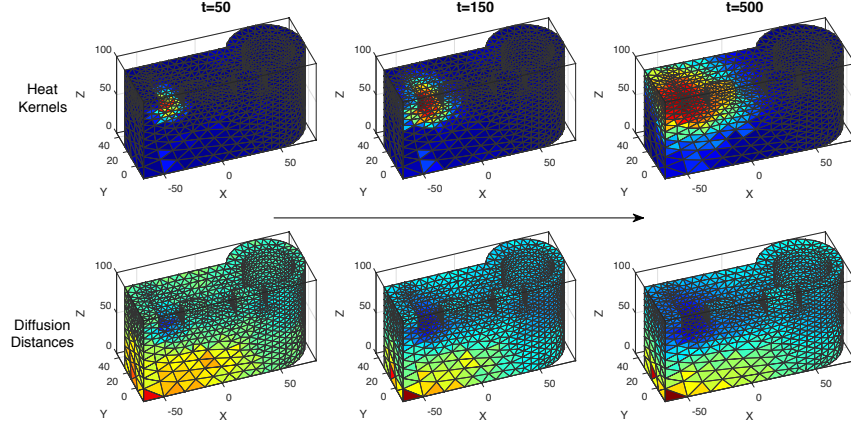


Figure 16: The heat kernel (top) and the diffusion distances plotted from a point on the triangulation of a part as time increases from left to right. Redder colors indicate higher values. The heat kernel values tend to a steady-state value as t diverges.

only the shortest path as the geodesic distances are, a property that has received recent attention in the Statistics and Manifold Learning literature (e.g., see Lee & Wasserman (2010)). This property is shared by heat kernels. This might be a *disadvantage* for SPC: changes in the mesh may reflect true changes in the shape of the parts that need to be detected. Figure 16 illustrates the evolution, for different values of t , of the heat kernels and diffusion distances from a point on the part shown in earlier figures, given the spectrum of its mesh. These are the quantities that were computed in the histograms of the last two columns of Figure 17, whose Q-Q plots in Figure 18 below. While the heat kernel can be easily understood as the diffusion in time of heat from a point, the diffusion distances have no easy interpretation from their time evolution plot shown in the figure.

Consider the three parts displayed on the leftmost column of Figure 17 (measurements in mm.), where (as before) we have added isotropic $N(0, 0.05^2 \mathbf{I}_3)$ noise to the points of a CAD model defined as a triangulation on a (rather small) point cloud with 1680 points. The euclidean distances between all points for the noise free and noisy parts are displayed in the second column; these histograms are invariant, but not intrinsic. The geodesic distances between all points, computed on the triangulation (using the “Fast marching algorithm” on the triangulation, see Kimmel (2004)) is displayed in the third column; this is both invariant and intrinsic.

Figure 18 shows Q-Q plots for two of the types of local defects studied before, the chipped part #1 shown in Figure 17, and the part with a protrusion on the edge at the top. Here the “in control” distributions of the heat kernels and diffusion distances are plotted against the distributions of the defective parts. We can see deviations from linearity in the profiles of both heat kernels and diffusion distances, but it is not clear what the role of the t parameter in the “detection” capabilities of a profile monitoring scheme would be. It seems plausible that smaller values of t allow to detect *local* changes better, while larger values of t would detect *global* changes better, but considerable more research is needed to assess this statement in order to provide useful tools for SPC.

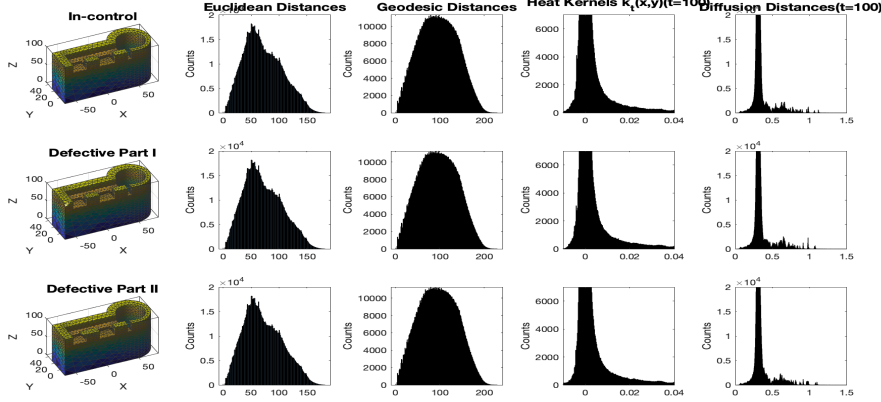


Figure 17: Histograms of the euclidean and geodesic distances, the heat kernels ($t = 100$) and diffusion distances ($t = 100$) for an in-control part (top row) and two types of parts with small local defects, a chipped corner (middle row) and a protrusion on the top of the part (bottom row).

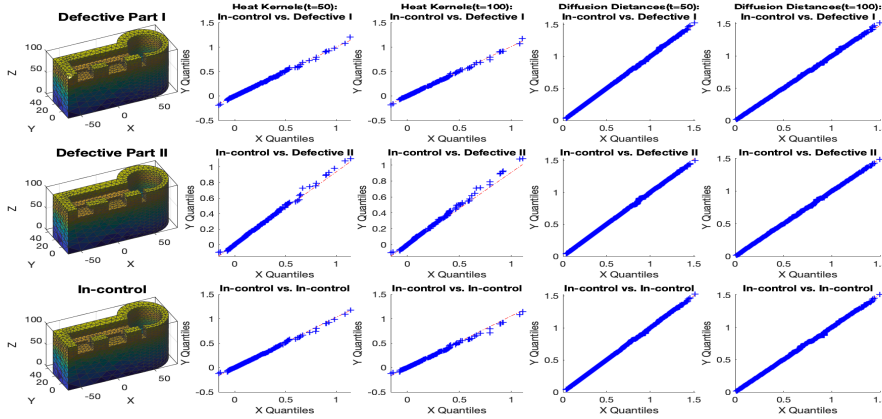


Figure 18: Q-Q plot of the heat kernels and diffusion distances between an in-control part and two types of parts with small local defects, a chipped corner (top row) and a protrusion on the top of the part (bottom row). Here, $t = 50$ (2nd and 4th column) and $t = 100$ (3rd and 5th columns).

7.2 Other spectral distances

Both the heat kernel and the diffusion distances, and the other spectral distances we describe next, can be used as an alternative criterion for registering two parts, using the “shape context” idea of Belongie *et al.* (2002) to find matches of points between two surfaces. The matches between points in a part that triggered an alarm and a CAD model could be then used as an additional post-alarm SPC diagnostic to determine where the produced part differs from acceptable ones, analogously to the ICP post-alarm diagnostic presented earlier (this would require more computational effort than using ICP, as it requires both finding the spectrum and solving the combinatorial registration problem, but could provide better information specially when the defect is small and not obvious to the eye). It is unclear, however, how to use these spectral distance tools without recourse to registration. It is also unclear how to set in practice the t parameter, present in both heat

kernel and diffusion distances.

There are, however, spectral distances that eliminate the t parameter. For a point x on a surface \mathcal{M} , Rustamov (2007) defines the “global point signature” (GPS) as the map of x into the infinite dimensional vector

$$\text{GPS}(x) = \left(\frac{1}{\sqrt{\lambda_1}}\phi_1(x), \frac{1}{\sqrt{\lambda_2}}\phi_2(x), \frac{1}{\sqrt{\lambda_3}}\phi_3(x), \dots \right)$$

In practice, the GPS embedding is finite dimensional using the lower part of the discrete LB spectrum and the associated eigenvectors. The idea of embedding a point from a manifold \mathcal{M} into a different dimensional space is a theme common to both Computer Graphics (e.g., “Heat Kernel Signatures” Sun *et al.* (2009a)), where a *higher* dimensional embedding is sought to define a similarity metric in that space between points originally in \mathbb{R}^3 , and Manifold Learning (see, e.g., Belkin & Niyogi (2002) “Laplacian eigenmaps”), where the goal is usually to find a *lower* dimensional embedding for understanding the data manifold structure. In the case of GPS, a distance function between two points on a 2-manifold can be defined by taking the inner product of their embeddings:

$$G(x, y) = \langle \text{GPS}(x), \text{GPS}(y) \rangle = \sum_{i=1}^{\infty} \frac{\phi_i(x)\phi_i(y)}{\lambda_i} \quad (14)$$

which can be obtained also as the integral of the heat kernel $k_t(x, y)$ with respect to t . A distance (metric) between $x, y \in \mathcal{M}$ is then given by $\sqrt{G(x, y)}$.

A distance (metric) related to the GPS distance is the so-called “Commute time distance”, defined as:

$$d_c(x, y)^2 = \sum_{i=1}^{\infty} \frac{(\phi_i(x) - \phi_i(y))^2}{\lambda_i}, \quad x, y \in \mathcal{M} \quad (15)$$

which is related to the GPS distance since $d_c(x, y)^2 = G(x, x) + G(y, y) - 2G(x, y)$. Lipman *et al.* (2010) indicate that both the GPS and the commute time distances have the disadvantage of diverging when $x = y$ since $\sum_{i=1}^{\infty} 1/\lambda_i \approx \sum_{i=1}^{\infty} 1/i$ diverges, and proposed instead a modification, called “biharmonic distance”:

$$d_b(x, y)^2 = \sum_{i=1}^{\infty} \frac{(\phi_i(x) - \phi_i(y))^2}{\lambda_i^2}, \quad x, y \in \mathcal{M} \quad (16)$$

which does not diverge when $x = y$ since $\sum_{i=1}^{\infty} 1/\lambda_i^2 \approx \sum_{i=1}^{\infty} 1/i^2 = \pi^2/6 < \infty$. In practice, all these distances would be computed using the lower part of the spectrum of the discrete LB operator, up to a given eigenvalue-eigenvector pair.

8 Conclusions and further work

We have presented a fundamentally new approach for the Statistical Process Control of discrete-part manufacturing processes based on intrinsic differential-geometric properties

of the sequence of parts produced. Our proposal brings SPC closer to computer graphics/vision methods. The SPC problem, however, is inherently different than the shape similarity problem from these other fields, given that contrary to them, a method to be useful for SPC must be able to distinguish small but significant shape and size differences in a sequence of very similar parts, avoiding false alarms but considering increments in noise a potential source of an out-of-control condition. In contrast, computer graphics/vision methods for shape similarity assessment typically aim to detect large shape differences in a manner that is robust with respect to any measurement noise, which is filtered out.

The main differential-geometric tool we use is the unnormalized spectrum of the discrete Laplace-Beltrami operator, cropped to consider only its lower part. We discussed two different discrete LB operator approximations which are symmetrizable (ensuring a real spectrum and providing computational advantages) and pointwise convergent (providing theoretical guarantees), and adopted the localized mesh Laplacian of Li *et al.* (2015) due to its sparseness. Other discrete approximations of the LB operator are also symmetrizable, based on Finite Element Methods (FEM, Reuter *et al.* (2006)), and we leave their study and comparison with the Localized Mesh Laplacian used here for future work. The LB-spectrum chart method is intrinsic and hence avoids registration of the parts, which is a hard to solve combinatorial problem.

Given the non-normality of the discrete LB spectrum, we proposed to use (with some modifications) a multivariate, nonparametric permutation-based control chart due to Chen *et al.* (2016) for on-line or “Phase II” SPC and a similar permutation and rank-based approach for the startup or “phase I” due to Capizzi & Masarotto (2017). Run length analyses and detection probability assessments, respectively, indicate the practical feasibility of the methods, even with relative large meshes (with tens of thousands of points) on a modest laptop computer. The on-line (phase II) method is especially sensitive to detect small changes in the shape or size of the surfaces, while providing an easy to tune in-control Average Run Length. The phase I method requires a principal component analysis of the spectrum of the parts, and we showed how just with a few PCAs it is sufficient to have excellent detection performance while controlling the false alarm probability. We compared our phase II method with a nonparametric univariate chart based on registration of the parts using the Iterated Closest Point (ICP) algorithm, using its objective function as a monitoring statistic, but found the LB-spectrum chart to be much more sensitive to detect process changes. An ICP-based method was presented to determine the localization of the defect on the part surface as a post-alarm diagnostic only to be used after the generic, or overall SPC mechanism provided by the LB spectrum chart, triggers an alarm.

We discussed other distance measures used in the computer graphics/vision fields for shape similarity assessment that are based on the LB operator eigendecomposition, such as heat kernel and diffusion distances which require the specification of a “time” parameter that is hard to select in practice for a specific part. The discussion included the more potentially beneficial “global point signature” and “biharmonic” distances, which do not require specifying a time parameter, but considerable more work is required to transform these techniques into usable SPC methods. We also wish to study in the future SPC methods based on the nodal domains of the manifold which use information encoded in the LB operator eigenvectors. The i -th nodal set is the set of points in a manifold where

the i -th eigenvector of the LB operator is zero. These are useful in computer graphics to segment a 3D object, given Courant’s nodal domain theorem, which indicates how the k -th eigenvector partitions the manifold in up to k disjoint domains.

We mostly focused in this paper on surface data, where the intrinsic dimension of the manifold is 2. Our methods carry over to the case of voxel data, where the intrinsic dimension of the manifold is 3. These are of particular interest in SPC of additive manufacturing data obtained via computed tomography scans of the part, in order to determine the inner features of printed parts. The intrinsically 3-manifold data can be represented with a tetrahedralization, and FEM methods exist for approximating the LB operator from such data structure (Reuter *et al.* , 2007), thus we will consider voxel extensions of our methods in future work.

Finally, we briefly touched in this paper the topological information carried by the LB spectrum. In the future we wish to explore this information in conjunction with topological data analysis techniques for SPC of parts where the number of their holes needs to be monitored. Again, this is of particular interest in some additive manufacturing applications, such as bone implants in medical research, or parts made of lightweight materials in aerospace design.

Acknowledgement.- This research was partially supported by NSF grant CMMI 1537987.

SUPPLEMENTARY MATERIAL

Matlab code for the computation of the Localized Mesh Laplacian and for the modified DFEWMA control chart in the examples.

Data set: Prototypical part CAD model and CAD model for cylinder (mesh data), both in-control noise-free and noise-free defect versions included.

References

- Belkin, M. 2003. *Problems of Learning in Manifolds, Ph.D. Thesis, Computer Science Department, The University of Chicago.*
- Belkin, M., & Niyogi, P. 2008. Towards a theoretical foundation for Laplacian-based manifold methods. *Journal of Computer and System Sciences*, **74**(8), 1289–1308.
- Belkin, M., Sun, J., & Wang, Y. 2008. Discrete laplace operator on meshed surfaces. *Pages 278–287 of: Proceedings of the twenty-fourth annual symposium on Computational geometry.* ACM.
- Belkin, Mikhail, & Niyogi, Partha. 2002. Laplacian eigenmaps and spectral techniques for embedding and clustering. *Pages 585–591 of: Advances in neural information processing systems.*

- Belkin, Mikhail, Sun, Jian, & Wang, Yusu. 2009. Constructing Laplace operator from point clouds in \mathbb{R}^d . *Pages 1031–1040 of: Proceedings of the twentieth annual ACM-SIAM symposium on Discrete algorithms*. Society for Industrial and Applied Mathematics.
- Belongie, S., Malik, J., & Puzicha, J. 2002. Shape matching and object recognition using shape contexts. *IEEE Transactions on Pattern Analysis and Machine Intelligence*, 509–522.
- Besl, P.J., & McKay, N. D. 1992. A Method for registration of 3-D shapes. *IEEE Transactions on Pattern Analysis and Machine Intelligence*, **14**(2), 239–256.
- Box, G.E.P., & Ramírez, J. 1992. Cumulative score charts. *Quality and Reliability Engineering International*, **8**, 17–27.
- Buser, P. 1992. *Geometry and Spectra of Compact Riemann Surfaces*. Boston, MA.: Birkhauser.
- Buser, P., Conway, J., Doyle, P., & Semmler, K. D. 1994. Some planar isospectral domains. *International Mathematics Research Notices*, **391**(9).
- Capizzi, Giovanna, & Masarotto, Guido. 2017. Phase I distribution-free analysis of multivariate data. *Technometrics*, **59**(4), 484–495.
- Chavel, Isaac. 1984. *Eigenvalues in Riemannian geometry*. Vol. 115. Academic Press.
- Chen, N., Zi, X., & Zou, C. 2016. A Distribution-Free Multivariate Control Chart. *Technometrics*, **58**(4), 448–459.
- Chung, F.R.K., & Lu, L. 2006. *Complex Graphs and Networks*. American Mathematical Society.
- Colosimo, Bianca Maria. 2018. Modeling and monitoring methods for spatial and image data. *Quality Engineering*, **30**(1), 94–111.
- del Castillo, Enrique, & Colosimo, Bianca M. 2011. Statistical shape analysis of experiments for manufacturing processes. *Technometrics*, **53**(1), 1–15.
- Dey, Tamal K, Ranjan, Pawas, & Wang, Yusu. 2010. Convergence, stability, and discrete approximation of Laplace spectra. *Pages 650–663 of: Proceedings of the twenty-first annual ACM-SIAM symposium on Discrete algorithms*. Society for Industrial and Applied Mathematics.
- Dryden, I. L., & Mardia, K. 2016. *Statistical Shape Analysis with Applications in R, 2nd edition*. Wiley.
- Farnum, N. R. 1994. *Modern Statistical Quality Control and Improvement*. Belmont, CA: Duxbury press.
- Gordon, C., Webb, D.L., & Wolpert, S. 1992. One cannot hear the shape of a drum. *Bulleting of the American Mathematical Society*, **27**(1), 134–138.

- Kac, M. 1966. Can one hear the shape of a drum? *The American Mathematical Monthly*, **73**, part II, 1–23.
- Kendall, D. G. 1984. Shape Manifolds, Procrustean Metrics, and Complex Projective Spaces. *Bulletin of the London Mathematical Society*, **16**, 81–121.
- Kimmel, R. 2004. *Numerical geometry of images*. New York, NY: Springer-Verlag.
- Kreyszig, E. 1991. *Differential Geometry*. Differential Geometry. Dover Publications.
- Lee, Ann B, & Wasserman, Larry. 2010. Spectral connectivity analysis. *Journal of the American Statistical Association*, **105**(491), 1241–1255.
- Lele, S.R. 1993. Euclidean distance matrix analysis (EDMA): estimation of mean form and mean form difference. *Mathematical Geology*, **25**(5), 573–602.
- Levy, B. 2006. Laplace-Beltrami Eigenfunctions. Towards an Algorithm that “understands” geometry. *Proceedings of the IEEE International Conference on Shape Modeling and Applications (SMI '06)*.
- Li, X, Xu, G., & ZHANG, Y.J. 2015. Localized discrete Laplace-Beltrami operator over triangluar mesh. *Computer Aided Geometric Design*, **39**, 67–82.
- Lipman, Yaron, Rustamov, Raif M, & Funkhouser, Thomas A. 2010. Biharmonic distance. *ACM Transactions on Graphics (TOG)*, **29**(3), 27.
- Liu, Yang, Prabhakaran, Balakrishnan, & Guo, Xiaohu. 2012. Point-based manifold harmonics. *IEEE Transactions on visualization and computer graphics*, **18**(10), 1693–1703.
- Newman, Mark. 2010. *Networks: an introduction*. Oxford university press.
- O’Neill, B. 2006. *Elementary Differential Geometry, 2nd ed.* Academic Press.
- Patané, G. 2014. Laplacian spectral distances and kernels on 3D shapes. *Pattern Recognition*, **47**, 102–110.
- Patané, Giuseppe. 2017. An introduction to laplacian spectral distances and kernels: theory, computation, and applications. *Page 3 of: ACM SIGGRAPH 2017 Courses*. ACM.
- Reuter, M., Wolter, F.E., & Peinecke, N. 2006. Laplace-Beltrami spectra as “Shape-DNA” of surfaces and solids. *Computer-Aided Design*, **38**(4), 342–366.
- Reuter, M., Niethammer, M, Wolger, F.E, Bouix, S., & Shenton, M. 2007. Global Medical Shape Analysis Using the Volumetric Laplace Spectrum. *2007 International Conference on Cyberworlds (CW’07)*, 417–426.
- Reuter, M., Wolter, F.E., Shenton, M., & M., Niethammer. 2009. Laplace-Beltrami eigenvalues and topological features of eigenfunctions for statistical shape analysis. *Computer-Aided Design*, **41**, 739–755.

- Rustamov, Raif M. 2007. Laplace-Beltrami eigenfunctions for deformation invariant shape representation. *Pages 225–233 of: Proceedings of the fifth Eurographics symposium on Geometry processing*. Eurographics Association.
- Sinha, Ayan, & Ramani, Karthik. 2014. Multi-Scale Kernels Using Random Walks. *Pages 164–177 of: Computer Graphics Forum*, vol. 33. Wiley Online Library.
- Sun, Jian, Ovsjanikov, Maks, & Guibas, Leonidas. 2009a. A concise and provably informative multi-scale signature based on heat diffusion. *Computer graphics forum*, **28**(5), 1383–1392.
- Sun, X., Rosin, P.L., R.R., Martin, & Langbein, F.C. 2009b. Noise analysis and synthesis for 3D laser depth scanners. *Graphical Models*, **71**(2), 34–48.
- Wardetzky, Max, Mathur, Saurabh, Kälberer, Felix, & Grinspun, Eitan. 2007. Discrete Laplace operators: no free lunch. *Pages 33–37 of: Symposium on Geometry processing*.
- Yang, P.C., & S.T., Yau. 1980. Eigenvalues of the laplacian of compact riemannian surfaces and minimal submanifolds. *Annali della Scuola Normale Superiore di Pisa, Classe di Scienze 4e série*, **7**(1), 55–63.
- Zhang, Z. 1992. *Iterative point matching for registration of free-form curves*. Tech. rept. Reports de Recherche no. 1658, INRIA, Sophia Antipolis, France,.

Appendix 1. Computation of the exact LB operator for a function defined on a Riemannian manifold

The following material can be found in many Differential Geometry books (e.g. Kreyszig (1991)).

where g is a symmetric $k \times k$ matrix defining the *metric tensor* on \mathcal{M} (giving the induced metric), with components given by entries g_{ij} and g^{ij} are the elements in matrix g^{-1} . The metric components g_{ij} can be obtained from the *first fundamental form* of \mathcal{M} Kreyszig (1991), which defines how arc length elements s on \mathcal{M} relate to the local coordinates of the manifold described parametrically by $\mathbf{x}(x^1, x^2, \dots, x^k)$:

$$ds^2 = \sum_{\alpha=1}^k \sum_{\beta=1}^k g_{\alpha\beta} dx^\alpha dx^\beta$$

If $k = 2$, the first fundamental form is given by the quadratic form:

$$ds^2 = g_{11}(dx^1)^2 + 2g_{12}dx^1dx^2 + g_{22}(dx^2)^2$$

from where $g = [g_{ij}]$ is a 2×2 matrix, that is, the first fundamental form defines the Riemannian metric g on \mathcal{M} , allowing to measure angles and areas on the manifold. (Note: common notation in many books is $E = g_{11}$, $F = g_{12}$, and $G = g_{22}$).

Example.- To illustrate the first fundamental form and the computation of the LB operator, consider a Torus in \mathbb{R}^3 described parametrically by:

$$\mathbf{x}(u, v) = ((R + r \cos v) \cos u, (R + r \cos v) \sin u, r \sin v)$$

where the surface coordinates are $x^1 = u$ and $x^2 = v$ (see Figure ??) and where R is the outer radius and r is the inner radius. Then, $g_{11} = (R + r \cos v)^2$, $g_{12} = 0$ and $g_{22} = r^2$, and the first fundamental form is:

$$ds^2 = (R + r \cos v)^2 (dx^1)^2 + r^2 (dx^2)^2$$

Figure 19 shows an example of the Torus for $R = 3, r = 1$ in the usual parametrization.

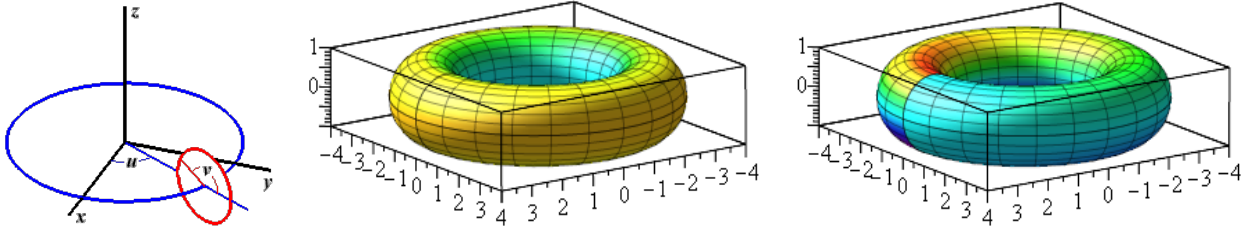


Figure 19: From left to right: Torus parametrization, and torus ($R = 3, r = 1$) colored according to $\Delta_{\mathcal{M}} f$ for $f = u^2$ and $f = u \cdot v$. Red and blue represent highest to lowest function values respectively. The LB operator on $f = u^2$ is not a function of u , the “horizontal” angle, so note how it is constant for each u , varying only transversally to the “tube” as a function of v . For $f = u \cdot v$, in contrast, the Laplacian is a function of both u and v .

Consider the function $f = u^2$ defined on the Torus \mathcal{M} . The LB operator applied on f equals the scalar:

$$\Delta_{\mathcal{M}} f = \frac{2}{(R + r \cos v)^2}$$

which is only a function of v (Figure 19, middle). If $f = u \cdot v$ instead, its Laplacian is:

$$\Delta_{\mathcal{M}} f = -\frac{u \sin v}{(R + r \cos v)r}$$

which varies as a function of both angles (Figure 19, right) ■.

Appendix 2. The heat kernel and the mesh (triangulation) approximation to the LB operator

A heat diffusion process over \mathcal{M} , the surface of a 3D object, is governed by the *heat equation* or (diffusion equation):

$$\Delta_{\mathcal{M}} u(x, t) = -\frac{\partial u(x, t)}{\partial t}$$

where $\Delta_{\mathcal{M}}$ is the LB operator on \mathcal{M} and $u(x, t)$ is the temperature at x at time t . The heat equation intuitively says that the rate of change in time of the temperature is proportional

to the “curvature” of u in \mathcal{M} . Given an initial heat distribution $u(x, 0) = f : \mathcal{M} \Rightarrow \mathbb{R}$, the solution to the heat equation is given by the integral equation

$$u(x, t) = H_t f(x) = \int_{\mathcal{M}} k_t(x, y) f(y) dy$$

where the bilinear function $k_t(x, y) : \mathbb{R}^+ \times \mathcal{M} \times \mathcal{M} \rightarrow \mathbb{R}$ is called the *heat kernel* which can be thought of as the amount of heat transmitted from x to y in time t if there is a unit heat source at x and where dy stands for area (of \mathcal{M}) and H_t is called the *heat operator*.

In case when $\mathcal{M} = \mathbb{R}^2$, the heat kernel is given by the Gaussian function Belkin & Niyogi (2008):

$$k_t(x, y) = (4\pi t)^{-1} e^{-\frac{\|x-y\|^2}{4t}}.$$

$u(x, t) = H_t f$ satisfies the heat equation: $\frac{\partial}{\partial t} u(x, t) + \Delta u(x, t) = 0$. In case $\mathcal{M} \subset \mathbb{R}^n$, then the heat kernel can be obtained only after obtaining the spectrum of the LB operator, using expression (12).

Mesh Laplacian derivation

We show how the discrete Mesh Laplacian can be written as the matrix $L_K^t = D - W$. Define \mathcal{K} = given triangulation, T_K =set of all triangles in \mathcal{K} , V =set of all triangles in \mathcal{K} , $A(T)$, $V(T)$ =area and set of vertices of triangle T , The discrete Mesh Laplacian can be written as follows:

$$\begin{aligned} L_K^t f(p_i) &= \frac{1}{4\pi t^2} \sum_{T \in T_K} \frac{A(T)}{3} \sum_{p_j \in V(T)} e^{-\|p_i - p_j\|^2 / 4t} (f(p_i) - f(p_j)) \\ &= \frac{1}{4\pi t^2} \sum_{T \in T_K} \sum_{p_j \in V(T)} \frac{A(T)}{3} e^{-\|p_i - p_j\|^2 / 4t} (f(p_i) - f(p_j)) \\ &\quad \text{(For each triangle, look at all its vertices)} \\ &= \frac{1}{4\pi t^2} \sum_{p_j \in V} \sum_{T: p_j \in V(T)} \frac{A(T)}{3} e^{-\|p_i - p_j\|^2 / 4t} (f(p_i) - f(p_j)) \\ &\quad \text{(For each vertex, look at all triangles associated with it)} \\ &= \frac{1}{12\pi t^2} \sum_{p_j \in V} \sum_{T: p_j \in V(T)} A(T) e^{-\|p_i - p_j\|^2 / 4t} (f(p_i) - f(p_j)) \\ &= \left(\sum_{p_j \in V} \frac{1}{12\pi t^2} \sum_{T: p_j \in V(T)} A(T) e^{-\|p_i - p_j\|^2 / 4t} \right) f(p_i) \\ &\quad - \sum_{p_j \in V} \left(\frac{1}{12\pi t^2} \sum_{T: p_j \in V(T)} A(T) e^{-\|p_i - p_j\|^2 / 4t} \right) f(p_j) \end{aligned}$$

First we discretize function f on the data as a vector $f = (f(p_1) \ f(p_2) \ \dots \ f(p_m))^T$. Then let $W_{ij} = \frac{1}{12\pi t^2} \sum_{T: p_j \in V(T)} A(T) e^{-\|p_i - p_j\|^2 / 4t}$ and $D_{ii} = \sum_j W_{ij}$, we have

$$\begin{aligned}
L_K^t f(p_i) &= \left[D_{ii} f(p_i) - (W_{i1} \ W_{i2} \ \cdots \ W_{im}) \begin{pmatrix} f(p_1) \\ f(p_2) \\ \vdots \\ f(p_m) \end{pmatrix} \right] \\
&= \left[(0 \ 0 \ \cdots \ D_{ii} \ \cdots \ 0) \begin{pmatrix} f(p_1) \\ f(p_2) \\ \vdots \\ f(p_i) \\ \vdots \\ f(p_m) \end{pmatrix} - (W_{i1} \ W_{i2} \ \cdots \ W_{im}) \begin{pmatrix} f(p_1) \\ f(p_2) \\ \vdots \\ f(p_m) \end{pmatrix} \right]
\end{aligned}$$

Define $D = \text{diag}[D_{ii}]$ and $W = [W_{ij}]$, then $L_K^t f = (D - W)f$ and $L_K^t = D - W$. This is in agreement with the Graph Laplacian, defined as $L = D - W$ where the weights W are given by the adjacency matrix of the graph.

Appendix 3. Exact moments for DFEWMA chart statistic

The expression for $T_{jn}(w, \lambda)$ in Chen *et al.* (2016), assuming to simply be a weighted sum of the standardized ranks, has an extra w in the numerator (the mean), and the denominator (the variance) is only correct for $\lambda = 0$. Since the test statistic is a weighted sum, the *covariances* between the terms added need to be considered, so here we derive the exact moments needed in expression (11).

Suppose we have m_0 parts from phase I and n parts from phase II. Altogether we have $m_0 + n$ parts labeled as $\{-m_0 + 1, -m_0 + 2, \dots, 0, 1, \dots, n\}$. Given the current window size w , for component j , we test the rank statistic $\sum_{i=n-w+1}^n (1 - \lambda)^{n-i} R_{jni}$, where R_{jni} is the rank of X_{ji} among $\{X_{j,-m_0+1}, X_{j,-m_0+2}, \dots, X_{j,n}\}$.

Under the null hypothesis (all parts are from the same distribution so R_{jni} can be any number from 1 to $m_0 + n$ with equal probability),

$$E[R_{jni}] = \frac{m_0 + n + 1}{2}, \quad \text{Var}(R_{jni}) = \frac{(m_0 + n + 1)(m_0 + n - 1)}{12}$$

The test statistic is then:

$$T_{jn}(w, \lambda) = \frac{\sum_{i=n-w+1}^n (1 - \lambda)^{n-i} R_{jni} - E \left[\sum_{i=n-w+1}^n (1 - \lambda)^{n-i} R_{jni} \right]}{\sqrt{\text{Var} \left(\sum_{i=n-w+1}^n (1 - \lambda)^{n-i} R_{jni} \right)}}$$

where

$$\begin{aligned}
E \left[\sum_{i=n-w+1}^n (1-\lambda)^{n-i} R_{jni} \right] &= \sum_{i=n-w+1}^n (1-\lambda)^{n-i} E[R_{jni}] \\
&= \sum_{i=n-w+1}^n (1-\lambda)^{n-i} \frac{m_0 + n + 1}{2} \\
&= L_1(\lambda, w) \frac{m_0 + n + 1}{2}
\end{aligned}$$

and where $L_1(\lambda, w) = \frac{1-(1-\lambda)^w}{\lambda}$, such that $\lim_{\lambda \rightarrow 0} L_1(\lambda, w) = w$.

We then have that:

$$\begin{aligned}
\lim_{\lambda \rightarrow 0} E \left[\sum_{i=n-w+1}^n (1-\lambda)^{n-i} R_{jni} \right] &= E \left[\sum_{i=n-w+1}^n R_{jni} \mid \lambda = 0 \right] \\
Var \left(\sum_{i=n-w+1}^n (1-\lambda)^{n-i} R_{jni} \right) &= \sum_{i=n-w+1}^n (1-\lambda)^{2(n-i)} Var(R_{jni}) \\
&\quad + 2 \sum_{n-w+1 \leq i < k \leq n} Cov((1-\lambda)^{n-i} R_{jni}, (1-\lambda)^{n-k} R_{jnk}) \\
&= \sum_{i=n-w+1}^n (1-\lambda)^{2(n-i)} Var(R_{jni}) \\
&\quad + 2 \sum_{n-w+1 \leq i < k \leq n} (1-\lambda)^{2n-i-k} Cov(R_{jni}, R_{jnk})
\end{aligned}$$

In particular, let $N = m_0 + n$ and consider:

$$\begin{aligned}
E[R_{jni} R_{jnk}] &= \sum_{a=1}^{N-1} \sum_{b=a+1}^N ab \frac{1}{N(N-1)/2} \\
&= \frac{2}{N(N-1)} \sum_{a=1}^{N-1} a \sum_{b=a+1}^N b \\
&= \frac{2}{N(N-1)} \sum_{a=1}^{N-1} a(a+N+1)(N-a)/2 \\
&= \frac{1}{N(N-1)} \sum_{a=1}^{N-1} [-a^3 - a^2 + a(N^2 + N)] \\
&= \frac{1}{N(N-1)} \frac{N(N^2-1)(3N+2)}{12} \\
&= \frac{(N+1)(3N+2)}{12} \\
Cov(R_{jni}, R_{jnk}) &= E[R_{jni} R_{jnk}] - E[R_{jni}] E[R_{jnk}] \\
&= \frac{(N+1)(3N+2)}{12} - \left(\frac{N+1}{2} \right)^2 \\
&= -\frac{N+1}{12} = -\frac{m_0+n+1}{12}
\end{aligned}$$

So when $\lambda \neq 0$,

$$\begin{aligned}
Var \left(\sum_{i=n-w+1}^n (1-\lambda)^{n-i} R_{jni} \right) &= \sum_{i=n-w+1}^n (1-\lambda)^{2(n-i)} Var(R_{jni}) \\
&+ 2 \sum_{n-w+1 \leq i < k \leq n} (1-\lambda)^{2n-i-k} Cov(R_{jni}, R_{jnk}) \\
&= \left(\sum_{i=n-w+1}^n (1-\lambda)^{2(n-i)} \right) \frac{(m_0+n+1)(m_0+n-1)}{12} \\
&- \left(\sum_{i=n-w+1}^{n-1} \sum_{k=i+1}^n (1-\lambda)^{2n-i-k} \right) \frac{m_0+n+1}{6} \\
&= \frac{1-(1-\lambda)^{2w}}{2\lambda-\lambda^2} \frac{(m_0+n+1)(m_0+n-1)}{12} \\
&- \left(\frac{1-\lambda-(1-\lambda)^w}{\lambda^2} - \frac{(1-\lambda)^2-(1-\lambda)^{2w}}{\lambda^2(2-\lambda)} \right) \frac{m_0+n+1}{6} \\
&= L_2(\lambda, w) \frac{(m_0+n+1)(m_0+n-1)}{12} + L_3(\lambda, w) \frac{m_0+n+1}{6}
\end{aligned}$$

We also have that

$$\lim_{\lambda \rightarrow 0} L_2(\lambda, w) = w$$

and

$$\lim_{\lambda \rightarrow 0} L_3(\lambda, w) = \frac{w(w-1)}{2}$$

so that

$$\lim_{\lambda \rightarrow 0} Var \left(\sum_{i=n-w+1}^n (1-\lambda)^{n-i} R_{jni} \right) = \frac{w(m+n+1)(m_0+n+w)}{12} = Var \left(\sum_{i=n-w+1}^n R_{jni} \mid \lambda = 0 \right)$$

When $\lambda = 0$ the variance reduces to:

$$\begin{aligned}
Var \left(\sum_{i=n-w+1}^n (1-\lambda)^{n-i} R_{jni} \right) &= \sum_{i=n-w+1}^n (1-\lambda)^{2(n-i)} Var(R_{jni}) \\
&+ 2 \sum_{n-w+1 \leq i < k \leq n} (1-\lambda)^{2n-i-k} Cov(R_{jni}, R_{jnk}) \\
&= w \frac{(m_0+n+1)(m_0+n-1)}{12} - 2 \frac{w(w-1)}{2} \frac{m_0+n+1}{12} \\
&= \frac{w(m_0+n+1)(m_0+n-w)}{12}
\end{aligned}$$

Therefore, summarizing, the variance equals to:

$$Var \left(\sum_{i=n-w+1}^n (1-\lambda)^{n-i} R_{jni} \right) = \begin{cases} \frac{w(m_0+n+1)(m_0+n-w)}{12} & \lambda = 0 \\ \frac{1-(1-\lambda)^{2w}}{2\lambda-\lambda^2} \frac{(m_0+n+1)(m_0+n-1)}{12} - \left(\frac{1-\lambda-(1-\lambda)^w}{\lambda^2} - \frac{(1-\lambda)^2-(1-\lambda)^{2w}}{\lambda^2(2-\lambda)} \right) \frac{m_0+n+1}{6} & \lambda \neq 0 \end{cases}$$

Finally, that $Var \left(\sum_{i=n-w+1}^n (1-\lambda)^{n-i} R_{jni} \right)$ is continuous in λ is easy to show:

$$\begin{aligned}
\lim_{\lambda \rightarrow 0} Var \left(\sum_{i=n-w+1}^n (1-\lambda)^{n-i} R_{jni} \right) &= \lim_{\lambda \rightarrow 0} L_2(\lambda, w) \frac{(m_0 + n + 1)(m_0 + n - 1)}{12} + \lim_{\lambda \rightarrow 0} L_3(\lambda, w) \frac{m_0 + n + 1}{6} \\
&= w \frac{(m_0 + n + 1)(m_0 + n - 1)}{12} - \frac{w(w-1)}{2} \frac{m_0 + n + 1}{6} \\
&= \frac{w(m_0 + n + 1)(m_0 + n - 1)}{12} - \frac{w(w-1)(m_0 + n + 1)}{12} \\
&= \frac{w(m_0 + n + 1)(m_0 + n - 1 - w + 1)}{12} \\
&= \frac{w(m_0 + n + 1)(m_0 + n - w)}{12} = Var \left(\sum_{i=n-w+1}^n R_{jni} \mid \lambda = 0 \right)
\end{aligned}$$